





RESEARCH ARTICLE | NOVEMBER 21 2023

An analytical model of the dynamics of reattaching jets ^{EP}

Chris J. Nicholls ; Brian M. T. Tang ; James Turner ; Marko Bacic 



Physics of Fluids 35, 115134 (2023)

<https://doi.org/10.1063/5.0170567>



CrossMark

Physics of Fluids

Special Topic: Overview of Fundamental
and Applied Research in Fluid Dynamics in UK

[Submit Today](#)

An analytical model of the dynamics of reattaching jets

Cite as: Phys. Fluids **35**, 115134 (2023); doi: [10.1063/5.0170567](https://doi.org/10.1063/5.0170567)

Submitted: 3 August 2023 · Accepted: 18 September 2023 ·

Published Online: 21 November 2023



View Online



Export Citation



CrossMark

Chris J. Nicholls,^{a)}  Brian M. T. Tang,  James Turner,  and Marko Bacic 

AFFILIATIONS

Department of Engineering Science, University of Oxford, Oxford OX2 0ES, United Kingdom

^{a)} Author to whom correspondence should be addressed: christopher.nicholls@eng.ox.ac.uk

ABSTRACT

A jet that emerges from a nozzle and attaches to an inclined, setback wall is studied. The reattaching jet is the canonical element of most fluidic devices, and the aim of this paper is to improve the understanding of its dynamics. An analytical model is developed that describes the dynamic behavior of the jet position in response to acoustic excitation. A novel, unsteady jet curvature equation is derived from first principles, which forms the basis of the model. The Görtler velocity profile for a plane, turbulent jet is assumed, and an alternative approach to determining its virtual origin is used. A novel approach to modeling the momentum balance at the jet reattachment point is demonstrated to predict the observed behavior in response to acoustic excitation. The resulting model is linearized at a series of operating points informed by data from the literature at a range of flow rates, wall setback distances, and gas types. A Monte Carlo analysis is conducted to quantify the model sensitivity to parameter uncertainty. The bandwidth of the jet response to acoustic excitation is demonstrated to depend linearly on jet velocity.

© 2023 Author(s). All article content, except where otherwise noted, is licensed under a Creative Commons Attribution (CC BY) license (<http://creativecommons.org/licenses/by/4.0/>). <https://doi.org/10.1063/5.0170567>

NOMENCLATURE

Latin

A	State matrix of linearized system	J'_2	US recirculated momentum flux per unit depth
b	Nozzle width	J'_{loss}	Momentum flux per unit depth lost to wall through viscous shear in US control volume
B	Input vector of linearized system	L_1	Side length of attached side control volume around attachment point
C	Output vector of linearized system	L_2	Side length of unattached side control volume around attachment point
c_3	Constant ($c_3 = \frac{R_0 T}{M_m}$)	\dot{m}	Mass flow rate
d	Channel depth	M	Mach number
D	Attachment wall setback distance	m_{B1}	Mass of fluid in attached side bubble
$f(\theta)$	Volume of attached side bubble [$f(\theta) = V_{B1}$]	m_{B2}	Mass of fluid in unattached side bubble
$g(\theta)$	Radius of jet curvature [$g(\theta) = R$]	n	Number of standard volumes ($b^2 d$) in control port channel
$G(s)$	Transfer function representation of linearized system	N_{MC}	Number of model runs in Monte Carlo analysis
J	Nominal jet inlet momentum	p_{B1}	Attached side bubble pressure
\bar{J}	Inflated jet momentum integrated across nozzle exit	p_{B2}	Unattached side bubble pressure
J_{loss}	Momentum flux per unit depth lost to wall through viscous shear in AS control volume	p_∞	Ambient pressure
\bar{J}_{AS}	Jet momentum entering AS control volume	r	Radial coordinate of point in velocity profile measured from center of jet arc
\bar{J}_{US}	Jet momentum entering US control volume	R	Radius of jet curvature [$R = g(\theta)$], i.e., value of r at attachment point
J_1	AS forward momentum flux per unit depth	s	Distance along jet centerline from nozzle orifice
J'_1	US forward momentum flux per unit depth	t_{ShL}	Hyperbolic tangent of η_{ShL} [$t_{\text{ShL}} = \tanh(\eta_{\text{ShL}})$]
J_2	AS recirculated momentum flux per unit depth		

t_1	Hyperbolic tangent of η_1 [$t_1 = \tanh(\eta_1)$]
t_2	Hyperbolic tangent of η_2 [$t_2 = \tanh(\eta_2)$]
u	Velocity component parallel to jet centerline
u_{in}	Input to linearized system
$U_{in}(s)$	Input to linearized system in Laplace space
v	Velocity component normal to jet centerline
V_{const}	Constant volume shared by V_{B1} and V_{B2}
V_{B1}	Attached side bubble volume [$V_{B1} = f(\theta)$]
V_{B2}	Unattached side bubble volume
x	Streamwise distance along axis of nozzle
\mathbf{x}	State vector in linearized system
x_{co}	x -coordinate of corner between side wall and control port relative to center of nozzle orifice
x_{US}	Length of unattached side shear layer
y	Cross-stream coordinate, perpendicular to jet centerline to point in velocity profile
y_{out}	Output of linearized system
y_1	Cross-stream position of Streamline 1 (StL1)
y_2	Cross-stream position of Streamline 2 (StL2)
$Y_{out}(s)$	Output of linearized system in Laplace space
z	Coordinate perpendicular to nozzle axis
z_c	Temporally and spatially averaged Görtler profile centerline position
z_{co}	z -coordinate of corner between side wall and control port relative to center of nozzle orifice
Δp	Pressure difference across jet, $\Delta p = p_{B1} - p_{B2}$

Greek

α	Expansion angle of channel
β_1	Fraction of recirculated momentum exiting AS control volume at upstream boundary
β_2	Fraction of recirculated momentum exiting US control volume at upstream boundary
γ	Coefficient of $\dot{\theta}$ in JCE
$\Delta\sigma$	Difference between σ_{AS} and σ_{US} ($\Delta\sigma = \sigma_{AS} - \sigma_{US}$)
η	Nondimensional distance normal to jet centerline ($\eta = \frac{\sigma y}{s+s_0}$)
η_{ShL}	Value of η for edge of shear layer
η_1	Value of η for StL 1 at AS attachment point ($s = R\theta$)
η_2	Value of η for StL 2 at US attachment point ($s = x_{US}$)
ϵ	Fraction of σ_{\sim} included in AS bubble pressure dynamics
ϵ_0	Critical value of ϵ where DC gain sign changes
ϵ_1	Value of ϵ where system becomes NMP
κ	Shape factor
θ	Swept angle of the jet, i.e., value of ϕ at attachment point
ξ	Mass flow inflation constant
ζ	Coefficient of $\dot{\theta}$ in JCE
ρ	Density of jet
σ	Jet spread parameter
σ_{AS}	σ on attached side
σ_{US}	σ on unattached side
σ_{\sim}	Time-varying component of σ
ϕ	Polar angle coordinate of point in velocity profile measured relative to line perpendicular to nozzle axis

Abbreviations

AM	Amplitude modulation
----	----------------------

AR	Aspect ratio
AS	Attached side
CStL	Central streamline (jet centerline)
DSL	Dividing streamline
JCE	Jet curvature equation
NMP	Non-minimum phase
PIV	Particle image velocimetry
ShL	Shear layer
StL1	Streamline 1
StL2	Streamline 2
US	Unattached side

I. INTRODUCTION

This paper details the development of an analytical model to describe the dynamic behavior of a reattaching jet. Reattaching jets are a canonical element of fluidic devices based on the Coandă effect. Fluidic devices have attracted research interest for their potential as flow control actuators to solve problems such as separation control,¹ film cooling,² lift enhancement,³ noise control,⁴ and thrust vectoring.⁵ While a number of researchers have exploited the jet response to excitation,^{6–8} there has been little attempt to model jet dynamic behavior since the 1970s. The internal dynamics of jets have been studied with analytical tools such as linear stability analysis⁹ and with numerical investigations.^{10,11} In the present work, our interest is instead in modeling the dynamic behavior of the bulk jet. In the early years of fluidic devices, many modeling papers were written with the goal of understanding the jet attachment dynamics and predicting the switching time. After the initial enthusiasm for their application as fluid logic elements, efforts to model them have largely ended. Arwatz *et al.*,¹² Wang *et al.*,¹³ Saliba *et al.*,¹⁴ and Nicholls *et al.*¹⁵ have established relations to predict the oscillation frequency of passively controlled fluidic devices (oscillators). To the knowledge of the authors, no recent studies have attempted to model the dynamics of jet attachment.

Methods of actively controlling fluidic devices have included piezo-electric flaps,¹⁶ a secondary fluid supply,¹⁷ plasma actuators,¹⁸ and acoustic excitation.^{19–22} Tomac and Sundström^{23,24} have made strides to bring the oscillation frequency, sweep, and inclination angles of a sweeping jet fluidic oscillator under control by use of flow injection. Nicholls and Bacic²² have demonstrated the closed-loop control of the oscillation frequency and phase of a Spyropoulos-style²⁵ fluidic oscillator using solid-state piezoelectric buzzers as actuators. Control strategies have typically been restricted to open-loop schemes,^{19,26} which limit device performance in terms of the uncertainty in response time, the absence of disturbance rejection, and a lack of versatility of the achieved output waveform. This was demonstrated by Nicholls and Bacic,²⁷ where closing the loop reduced the uncertainty in the fluidic jet response time at the expense of the response bandwidth, and the output could be made to track an arbitrary reference signal. However, the dynamic model of the acoustically excited jet was a transfer function that was identified through a series of frequency response experiments parametrized with respect to flow rate. Such models cannot be used to understand the influence of geometric parameters on the jet dynamic behavior without additional experiments.

This paper aims to bridge the gap between the efforts to model fluidic devices in their early days and the renewed interest in their use for flow control applications. The goal is to develop a quantitative

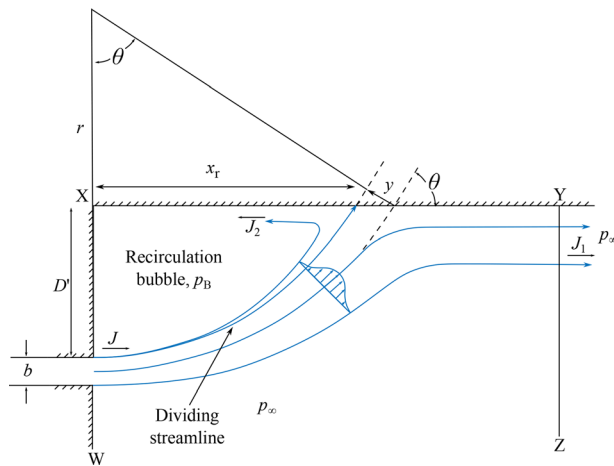


FIG. 1. Setback wall geometry considered by and with permission from Bourque and Newman, *Aeronaut. Q.* 11(3), 201–232. Copyright 1960 Royal Aeronautical Society.²⁹

understanding to facilitate their design and control. Focus is placed on the fundamental case of a reattaching jet, the component central to most Coandă-based fluidic devices. The means of actuation are acoustic, although the core model can be extended to other control methods.

When a jet issues from a nozzle (Fig. 1), as in a fluidic device, it entrains the surrounding ambient fluid, which causes it to spread out. If an adjacent wall that is set back and/or inclined from the axis of the nozzle confines one side of the jet, the entrainment flow on that side will be restricted and the pressure will decrease—this is the Coandă effect.²⁸ The pressure difference across the jet bends it toward the wall, which confines the wall-side further. Eventually, the jet strikes the wall, and a fraction of the main jet flow is recirculated into the bubble that forms in the now fully confined region. The recirculating flow stabilizes the pressure reduction due to entrainment, and a steady state is reached. The dividing streamline (DSL) separates the portion of the jet that recirculates into the bubble from that which continues downstream. Chapman *et al.*³⁰ studied the flow over a backward-facing step (Fig. 2) and suggested that particles on the free-stream side of the dividing streamline [green shaded region in Fig. 2(b)] have sufficient

energy to overcome the adverse pressure gradient along the wall, whereas those on the wall side of the dividing streamline (red shaded region) do not and are drawn into the bubble. Particles on the dividing streamline represent the limiting case and stagnate against the wall. In the steady state, continuity implies that the DSL must originate at the corner of the step.

Bourque and Newman²⁹ modeled an attached jet (Fig. 1) with the Görtler velocity profile for a plane turbulent jet (2)–(4) using momentum balance equations to resolve the jet at the attachment point. The Görtler profile is only valid far enough downstream of the nozzle orifice for the large-scale turbulent structures in the jet shear layer to have broken down into isotropic turbulence.³¹ Sawyer³² acknowledged this fact and used an error function velocity profile for the length of the jet potential core, which he then matched to a Görtler profile at the end of the potential core. It was shown by Sawyer³² that a near-symmetric jet profile can support different entrainment rates on each side due to the centrifugal forces associated with its curvature, while maintaining the overall plane jet entrainment rate suggested by Reichardt.³³

Müller³⁴ considered an attached jet in a fluidic device controlled by a second, perpendicular flow that filled the recirculation bubble transiently to detach the jet from the wall. Müller made a distinction between dynamic and steady switching. In the steady case, the control flow expanded the recirculation bubble until it reached some critical value required for detaching the jet from the wall. In the dynamic case, Müller described how the (larger) control flow caused a concentration of pressure adjacent to the port, resulting in a non-uniform jet curvature with respect to streamwise distance. This affected the balance of entrainment and recirculated flows, thereby affecting the jet detachment time. Lush^{35,36} considered the same setup and assumed that the jet was quasi-steady, which means that the relationship between the curvature and the transverse pressure difference derived from the Euler equation,

$$-\frac{J}{R} = \Delta p, \quad (1)$$

was assumed to hold in the transient. In Eq. (1), J is the jet momentum flux per unit depth, R is the radius of curvature of the jet centerline, and Δp is the pressure difference across the jet. The same assumption has been used in both steady-state^{29,37–39} and dynamic^{35,36,39–41} jet attachment models. The assumption that the Euler equation is

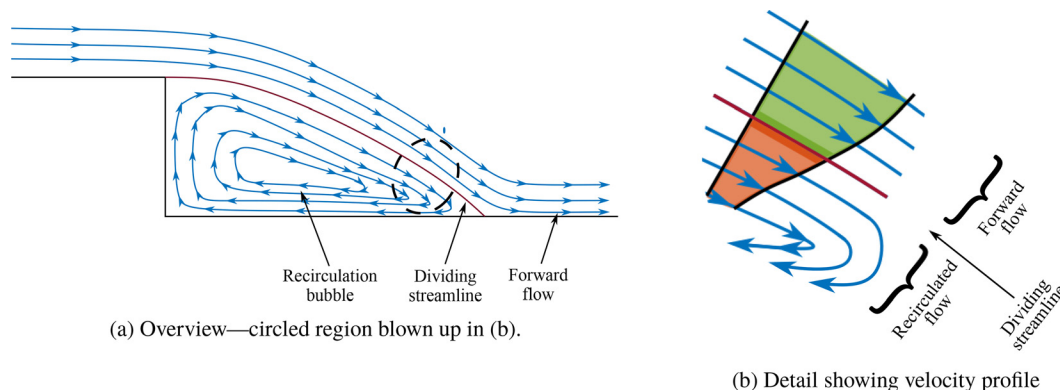


FIG. 2. Sketch of setup studied by Chapman *et al.*,³⁰ highlighting dividing streamline.

applicable to a time-varying jet was suggested by Kirshner and Katz⁴² to be the greatest source of inaccuracy in all previous models. One contribution of the present study is the derivation of an unsteady jet curvature equation to account for the bulk jet dynamics that are ignored by the use of Eq. (1).

Experimental results confirm that the effect of acoustic excitation is to increase the spreading of a jet.⁴³ The cause is the increase in entrainment that is driven by enhanced vorticity in the shear layer.^{43–45} It has further been shown that acoustically exciting a reattaching jet from the unattached side causes a biased increase in entrainment—the unattached side entrainment rate increases more than that on the attached side—and hence a lateral imbalance in jet spreading.¹⁹ Wiltse and Glezer⁷ perturbed a square jet using a piezoelectric flap that resonated at a frequency above the band to which the flow was receptive. The resonant frequency was used as a carrier tone, which was amplitude-modulated with a relatively low-frequency signal. Vortices were created at the carrier tone, which underwent merging events to produce larger vortices at the modulating frequency. As such, the jet shear layer demodulated the perturbation. The demodulated low-frequency signal was amplified by the shear layer, while the carrier tone signal was attenuated. More recently, Nicholls *et al.*⁴⁶ demonstrated that merging is one of two demodulation mechanisms. The other mechanism is based on the relationship between the vortex train and the corresponding shear layer vorticity signal, which was modeled as a half-wave rectification operation—a common implementation of a demodulator in communications systems (see Ref. 47, p. 157). This rectification model has been verified experimentally.⁴⁸ The shear layer demodulation property has been applied to achieve dynamic fluid jet control in the context of fluidic amplifiers²⁷ and fluidic oscillators.²² The present work builds on this by developing an analytical model to enhance the understanding of reattaching jet dynamics in response to acoustic perturbation.

In Sec. II, a novel unsteady jet curvature equation is derived from first principles, around which a dynamic model of an attached jet is constructed. In Sec. III, an analysis of the model is presented, consisting of a linearization and Monte Carlo analysis. Section IV provides a discussion of the modeling choices and the model output, as well as further analysis. Conclusions are drawn in Sec. V.

II. DYNAMIC MODEL

The geometry of the system being studied is shown in Fig. 3. The coordinates (s, y) describe a point in the jet velocity profile along and normal to the jet centerline, respectively, while (x, z) are parallel and perpendicular to the axis of the nozzle, respectively. The assumptions are as follows:

1. The jet centerline follows a circular arc with radius $R = R(t)$;
2. The width of the jet is small compared with the radius of the jet centerline;
3. The jet has a Görtler velocity profile;
4. The pressure inside the recirculation bubbles on both sides of the jet is spatially constant;
5. The fluid in the recirculation bubbles behaves as an ideal gas;
6. The jet has constant density.

Assumption (1) follows directly from assumption (4), which is discussed and justified in Sec. IV A. Calculations presented in Sec. III based on the data of Bourque and Newman²⁹ and Sawyer³⁷ indicate a

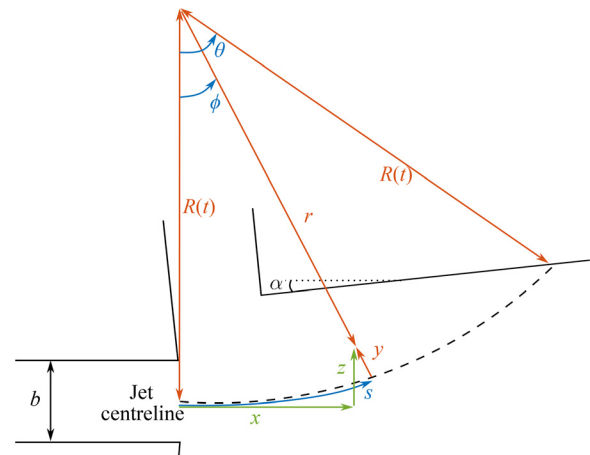


FIG. 3. Device diagram: basic geometry.

ratio of the jet radius of curvature to the nozzle width in the range 12–18 for the device dimensions most consistent with a fluidic device. In our own validation study (presented in a separate paper), the ratio was found to lie between 16 and 18, which justifies assumption (2). As regards assumption (3), while it would potentially be more accurate to follow the approach taken by Sawyer³² of matching the Görtler profile to some initial profile at the end of the potential core, this would add complexity. In this paper, the aim is to capture the important dynamics with the simplest possible description of the system. Assumption (5) is crucial for a device based on the Coandă effect where entrainment-driven evacuation of the regions surrounding the jet is the principal cause of the pressure reduction. This is discussed further in Sec. IV A. Assumption (6) is justifiable for a low Mach number jet ($M < 0.3$), which is assumed here. It should be noted that fluidic devices are often operated at compressible flow conditions. The novel (incompressible) jet curvature equation derived herein is expected to diverge from the real behavior in that regime.

A. Görtler velocity profile

The Görtler profile describes a plane, turbulent jet that originates from a point, the virtual origin³¹ (Fig. 4). The mass flow rate, \dot{m} , starts at zero and grows by the entrainment of ambient fluid at a rate proportional to the square root of the streamwise distance from the virtual origin. The virtual origin is selected so that the mass flow rate matches

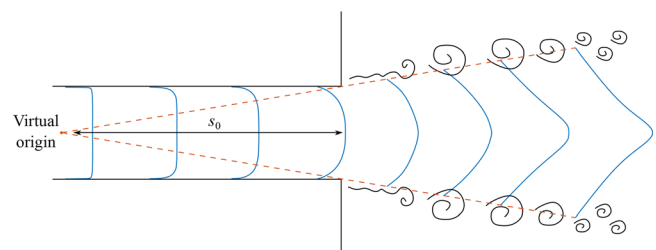


FIG. 4. Jet issuing from finite nozzle with velocity profile developing into the Görtler profile. The distance from the virtual origin to the nozzle orifice is s_0 .

that of the physical jet at the nozzle orifice. The equations describing the Görtler profile³¹ are

$$u = \frac{1}{2} \sqrt{\frac{3J\sigma}{\rho(s+s_0)}} \operatorname{sech}^2(\eta), \quad (2)$$

$$v = \frac{1}{4} \sqrt{\frac{3J}{\rho\sigma(s+s_0)}} [2\eta \operatorname{sech}^2(\eta) - \tanh(\eta)], \quad (3)$$

$$\eta = \frac{\sigma y}{s+s_0}, \quad (4)$$

where u and v are the streamwise and transverse velocities, σ is the jet spread parameter ($\sim 1/E$, where E is the entrainment rate), s is the distance along the jet centerline from the center of the inlet orifice, s_0 is the distance along the jet centerline from the virtual origin of the jet to the center of the inlet orifice, and y is the local coordinate perpendicular to the jet centerline at a given station s . The momentum flux per unit depth, J , is given by

$$J = \frac{\dot{m}^2}{\rho b d^2}, \quad (5)$$

where b and d are the nozzle width and depth, respectively.

B. Jet virtual origin

The jet virtual origin, s_0 , is typically set by matching the mass flow rate across the entire cross-stream domain of the Görtler profile to the mass flow of the physical jet that is being modeled, giving $s_0 = \sigma b/3$. This approach was introduced by Bourque and Newman.²⁹ The disadvantage is that it implies that the nozzle has infinite width and results in the incorrect mass flow across the actual nozzle width. The approach taken in the present work is to inflate the mass flow rate slightly by multiplying \dot{m} by a constant, ξ , in the definition of J in Eq. (5) and set the upper limit of the integral to $y = b/2$. This results in the correct mass flow across the nozzle at its exit, rather than the correct mass flow spread across the whole profile between $-\infty$ and ∞ . If \dot{m} in the expression for J in Eq. (5) is replaced with $\xi \dot{m}$, integrating the profile at $s = 0$ from $y = 0$ to $y = b/2$ and equating it to half the mass flow rate gives

$$\frac{\dot{m}}{2} = \int_0^{b/2} d\rho u dy = \int_0^{b/2} d\rho \left[\frac{3\xi^2 \dot{m}^2 \sigma}{4\rho^2 b d^2 (s+s_0)} \right]^{\frac{1}{2}} \operatorname{sech}^2 \left(\frac{\sigma y}{s+s_0} \right) dy. \quad (6)$$

The resulting Eq. (6), has a unique solution, $s_0 = 0.46\sigma b$, when $\xi = 1.07$. The argument for this approach is that it respects the fact that the nozzle has a finite width. The difference between the virtual origin in the present model, $s_0 = 0.46\sigma b$, and the traditional value, $s_0 = \sigma b/3$, is shown to have significant consequences for the dividing streamline.

C. Dividing streamline

The equation of the dividing streamline (DSL) can be derived from continuity, as in Bourque and Newman,²⁹ with the addition of the inflating factor ξ , and is given by

$$y_{\text{DSL}} = \frac{s+s_0}{\sigma} \operatorname{atanh} \left(\frac{1}{\xi} \sqrt{\frac{\sigma b}{3(s+s_0)}} \right). \quad (7)$$

This agrees with Bourque and Newman²⁹ if $\xi = 1$ and $s_0 = \sigma b/3$. The DSL as given by Eq. (7) with $\sigma = 12$ (a value typically used in the literature, for example, by Bourque and Newman²⁹ in their setback wall model) is plotted for these values of ξ and s_0 , as well as $\xi = 1.07$ and $s_0 = 0.46\sigma b$, in Fig. 5. The DSL using Bourque and Newman's virtual origin has $y_{\text{DSL}} \rightarrow \infty$ as $s \rightarrow 0$. On the other hand, the DSL from the present analysis is "well-behaved" and coincides with the edge of the nozzle at $y_{\text{DSL}} = b/2$. This represents a marked improvement over the traditional approach, which has been used extensively in the literature.^{35–40} It will be necessary later to evaluate the jet velocity profile at points along the DSL, which is possible when it is physically reasonable as in the present work. This is an advantage of the approach to define the virtual origin adopted in Sec. II B.

The normalized transverse velocity, v , given by $\bar{v} = 2\eta \operatorname{sech}^2(\eta) - \tanh(\eta)$, is plotted in Fig. 6. The function has roots at $\eta = \pm 1.09$, which come about as a result of (a) the jet spreading out from its centerline, such that the transverse velocity close to the centerline must have the same sign as η , and (b) the jet entraining flow from the surrounding fluid, such that far from the centerline, the transverse velocity must be toward the center of the jet, i.e., the opposite sign to η . The zero-crossings at $\eta = \pm 1.09$ are the edges of the shear layer, which are distinct from the DSLs. Beyond the edge of the shear layer in a free jet, the fluid has not been affected by the presence of the jet through viscous effects; i.e., it has not had streamwise momentum imparted on it through viscous shear. This is not reflected in the streamwise velocity profile, u , which only reaches 0 in the limit as $\eta \rightarrow \pm\infty$. The limits of the model domain are therefore taken to be the edges of the shear layer, defined by $\eta = \pm 1.09$.

For the model to be physically reasonable, the edge of the shear layer should coincide with the DSL at the edge of the nozzle orifice, then spread at a faster rate than the DSL. Otherwise, it would imply that a portion of the jet exists outside its own shear layer. To test this, the edge of the shear layer is constrained to pass through $y = b/2$ at $s = 0$, and the position of the jet virtual origin, s_0 , required to be

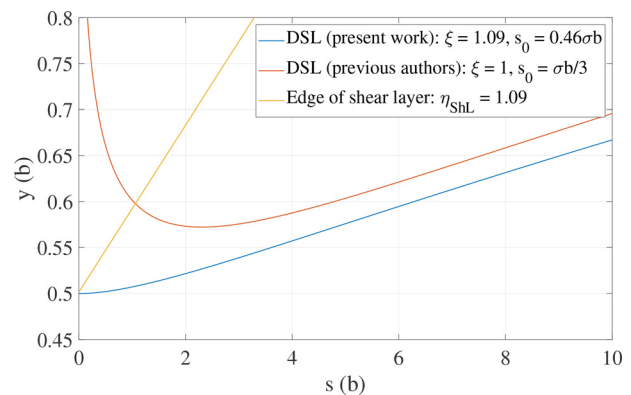


FIG. 5. Dividing streamline with $\xi = 1.07$ and $s_0 = 0.46\sigma b$ (present work, blue), $\xi = 1$ and $s_0 = \sigma b/3$ (previous authors, red), and edge of shear layer according to $\eta = 1.09$ (yellow). In all cases, $\sigma = 12$.

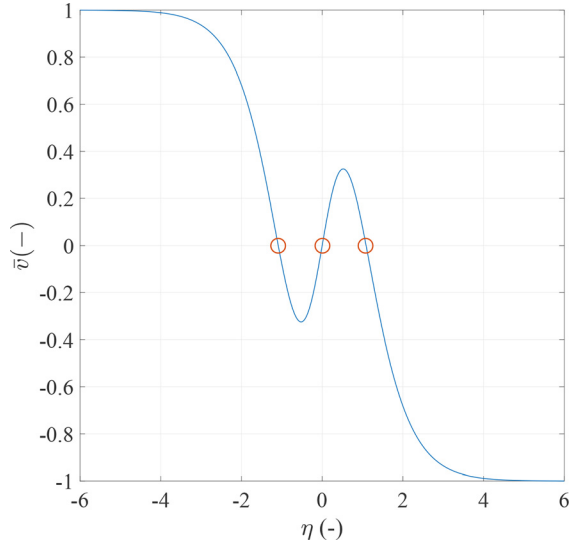


FIG. 6. Normalized transverse Görtler velocity profile, with zero-crossings marked in red circles.

achieved this is calculated. Substituting these values into the expression for η (4) and setting $\eta = \eta_{\text{shL}} = 1.09$ give

$$\eta = \frac{\sigma b}{2s_0} \Rightarrow s_0 = 0.46\sigma b, \quad (8)$$

which is in agreement with the previous calculation of s_0 . This demonstrates the agreement between the use of model domain boundaries given by η_{shL} , the inflation of the inlet mass flow by ζ , and the corresponding dividing streamline definition. Using this value of s_0 and $\sigma = 12$, the edge of the shear layer is plotted along with the dividing streamlines in Fig. 5. This value of s_0 leads to a physically reasonable dividing streamline that starts at the edge of the nozzle and represents the edge of the jet. It also gives a shear layer that grows from the edge of the nozzle and spreads faster than the dividing streamline.

D. Jet curvature equation

Ries⁴⁹ made attempts to develop an unsteady jet curvature equation, and the derivation presented here has a similar starting point, although a different conclusion is reached. The radial, incompressible Navier–Stokes momentum equation in polar coordinates is given by

$$\begin{aligned} \frac{\partial u_r}{\partial t} + u_r \frac{\partial u_r}{\partial r} + \frac{u_\phi}{r} \frac{\partial u_r}{\partial \phi} - \frac{u_\phi^2}{r} \\ = -\frac{1}{\rho} \frac{\partial p}{\partial r} + \frac{\mu}{\rho} \left[\frac{1}{r} \frac{\partial}{\partial r} \left(r \frac{\partial u_r}{\partial r} \right) - \frac{u_r}{r^2} + \frac{1}{r^2} \frac{\partial^2 u_r}{\partial \phi^2} - \frac{2}{r^2} \frac{\partial u_\phi}{\partial \phi} \right], \end{aligned} \quad (9)$$

where u_ϕ and u_r are the velocities parallel and perpendicular to the jet centerline, respectively. The diagram in Fig. 3 sets out the geometry referred to hereafter. Note that $s = R\phi$. It is assumed that the viscous terms are negligible and that there is no variation in radial velocity along the tangential direction, i.e., $\frac{\partial u_r}{\partial \phi} = R \frac{\partial u_r}{\partial s} = 0$. These assumptions are justified after the main derivation below. The expression $r = R - y$ can be seen from Fig. 3. Taking the time-derivative of this gives

$u_r = \dot{R} - v$, where $v = \frac{dy}{dt}$. It is noted that $u_\phi = u$, so that (u, v) are the local tangential and radial velocities at a point in the jet (s, y) . Substituting these expressions into Eq. (9), using $r = R - y$, and assuming $R \gg y$ leads to

$$\left(\ddot{R} - \frac{\partial v}{\partial t} \right) + (\dot{R} - v) \frac{\partial v}{\partial y} - \frac{u^2}{R} = \frac{1}{\rho} \frac{\partial p}{\partial y}. \quad (10)$$

Ries⁴⁹ took the integral with respect to y between the limits of $y = -\infty$ and $y = \infty$, and assumed that the pressure at $y = \infty$ is the bubble pressure, $p_{y=\infty} = p_B$, and that $p_{y=-\infty} = p_\infty$ on the other side of the jet at $y = -\infty$. The resulting equation is given by

$$[v]_{-\infty}^{\infty} \dot{R} - \frac{J}{\rho R} = \frac{1}{\rho} [p]_{-\infty}^{\infty}. \quad (11)$$

Ries⁴⁹ evaluates (incorrectly) $[v]_{-\infty}^{\infty} = +2$, where \bar{v} is the normalized transverse velocity. The form of the function v is shown in Fig. 6, which shows that $[v]_{-\infty}^{\infty} = -2$. Note that this is not simply a result of the different sign convention for y . Correcting this error results in a negative coefficient of $\frac{dR}{dt}$, which makes the resulting differential equation unstable (perturbations about the equilibrium value of R corresponding to a particular $[p]_{-\infty}^{\infty}$ result in $R \rightarrow 0$).

Returning to Eq. (10), there is a problem with setting the integration limits to $y = \pm\infty$, in that these limits do not represent the edges of the jet, and assuming $p_{y=\infty} = p_B$ asserts that the pressure far from the edge of the jet shear layer is relevant to the jet dynamics. Since the edge of the jet has been identified as the dividing streamline, here the limits are set to be $\pm y_{\text{DSL}}$, so that $p_{y_{\text{DSL}}} = p_B$. This gives

$$2y_{\text{DSL}} \ddot{R} - \left[\frac{1}{2} v^2 \right]_{-y_{\text{DSL}}}^{y_{\text{DSL}}} + [v]_{-y_{\text{DSL}}}^{y_{\text{DSL}}} \dot{R} - \frac{\bar{J}}{\rho R} = \frac{1}{\rho} [p]_{-y_{\text{DSL}}}^{y_{\text{DSL}}}, \quad (12)$$

where \bar{J} is the momentum of the jet integrated across the nozzle exit. Since R is spatially uniform, for consistency, the equation is averaged in s by integrating between $s = 0$ and the attachment point, $s = R\theta$, as in Ries.⁴⁹ For simplicity, the coefficient of the second-order term in Eq. (12), $2y_{\text{DSL}}$, is calculated by taking the mean of the values of y_{DSL} at $s = 0$ and $s = R\theta$. This is justified because y_{DSL} is approximately linear with respect to s (see Fig. 5), and yields the new coefficient for \ddot{R} , given by

$$\gamma = y_{\text{DSL}}|_{s=0} + y_{\text{DSL}}|_{s=R\theta}. \quad (13)$$

Substituting γ into (12) gives

$$\gamma \frac{d^2 R}{dt^2} + \zeta \frac{dR}{dt} - \frac{\bar{J}}{\rho R} = \frac{1}{\rho} \Delta p, \quad (14)$$

$$\zeta = \frac{1}{R\theta} \sqrt{\frac{bJ}{\rho}} \left[2 \ln(1 - \chi^2) + \frac{2(\chi^2 + 1) \text{atanh}(\chi)}{\chi} - \ln(\chi) \right]_{\chi_1}^{\chi_2}, \quad (15)$$

and

$$\chi_1 = \frac{1}{\zeta} \sqrt{\frac{\sigma b}{3s_0}}, \quad \chi_2 = \frac{1}{\zeta} \sqrt{\frac{\sigma b}{3(R\theta + s_0)}}. \quad (16)$$

Equation (14) is a novel jet curvature equation. It removes the need for the quasi-steady jet assumption by incorporating the dynamics of the jet centerline curvature in response to changes in the pressure difference, Δp , across the jet.

Justification of assumptions

The inertial term, $\frac{u_\phi}{r} \frac{\partial u_r}{\partial \phi}$, in Eq. (9) can be shown to vanish in the y -integral performed in the derivation as a result of the symmetry of the velocity profile and noting that $R = R(t)$. The viscous terms reduce to

$$-\frac{\mu}{\rho} \left(\frac{2y_{\text{DSL}} \dot{R}}{R^2} - \frac{2}{R} \left[v - \frac{1}{4} \sqrt{\frac{3\bar{J}}{\rho\sigma(s+s_0)}} \tanh(\eta) \right] \right)_{-y_{\text{DSL}}}^{y_{\text{DSL}}}. \quad (17)$$

The impact of these terms on the system dynamics depends heavily on the value of μ . For the jet velocities in practical fluidic devices, the contribution of viscous terms remains one order of magnitude smaller than the other contributions when the eddy viscosity ratio reaches $O(10^4)$, justifying their exclusion.

E. Bubble volumes

The bubble volumes (per unit depth) are given by

$$V_{B1} = f(\theta) = \frac{R^2}{2} \left(\theta - \sin^2(\theta) \tan(\alpha) - \frac{1}{2} \sin(2\theta) \right) + nb^2, \quad (18)$$

$$V_{B2} = V_{\text{const}} - V_{B1}, \quad (19)$$

where the attached side bubble volume, V_{B1} , was found geometrically, and the unattached side volume is assumed to share the channel volume with the attached side bubble and the jet (which is taken to have a constant volume), giving the simple expression for V_{B2} above. The model results proved insensitive to the assumptions concerning the calculation of V_{B2} . The wall incline angle is given by α , and n is a constant related to the volume per unit depth of the control port channel. In reality, the control port in a fluidic device has dynamics—the pressure in the control port does not track the bubble pressure uniformly and without lag. In the present work, the control port dynamics were not included in the model because they depend strongly on its size and shape. In this study, the goal was to keep the model general. As such, a representative volume, nb^2d , was added to the bubble volume to account for the control port. In practice, with this simple model, the added volume should be somewhere between zero and the geometric volume of the control port, depending on the restriction provided by the port.

F. Ideal gas law

The ideal gas law is applied to both the attached and unattached side bubbles, denoted by subscripts B1 and B2, respectively, giving

$$p_{B1} = \left(\frac{R_0 T}{M_m} \right) \frac{m_{B1}}{V_{B1}}, \quad (20)$$

where M_m is the molar mass of air, R_0 is the universal gas constant, T is the temperature of the gas, and m_{B1} is the mass in bubble i . This approach (applied to one side) was taken by Ries.⁴⁹ The pressure difference term in the jet curvature equation (14) is given by $\Delta p = p_{B1} - p_{B2}$. Differentiating (20) with respect to time and substituting expressions for V_{B1} and V_{B2} leads to

$$\frac{dp_{B1}}{dt} = \frac{1}{f} \left[\left(\frac{R_0 T}{M_m} \right) \frac{dm_{B1}}{dt} - p_{B1} f' \dot{\theta} \right], \quad (21)$$

$$\frac{dp_{B2}}{dt} = \frac{1}{V_{\text{const}} - f} \left[\left(\frac{R_0 T}{M_m} \right) \frac{dm_{B2}}{dt} + p_{B2} f' \dot{\theta} \right]. \quad (22)$$

G. Mass flows on the attached side

The mass in the attached side bubble is given by the time integral of the difference between the entrainment and recirculation mass flows on this side, which are found with reference to Fig. 7. Streamline 1 (StL1) is the dividing streamline with respect to the downstream flow; it separates the recirculating flow (with momentum J_2) from the flow that continues downstream (with momentum J_1). The DSL is the dividing streamline with respect to the upstream flow; i.e., it divides flow exiting the nozzle orifice from recirculated flow. In the general, unsteady case, StL1 differs from the DSL, while in the steady state, they are identical. The entrainment mass flow rate (per unit depth) on the attached side can be found by integrating the velocity profile between the dividing streamline and the edge of the shear layer at the attachment point ($s = R\theta$), given by

$$\dot{m}_{e1} = \rho \int_{y_{\text{DSL}}}^{y_{\text{ShL}}} u dy = \frac{\dot{m}}{2} \left(\sqrt{\frac{3\zeta^2(R\theta + s_0)}{b\sigma}} \tanh(\eta_{\text{ShL}}) - 1 \right), \quad (23)$$

where $\eta_{\text{ShL}} = 1.09$. The recirculated flow (per unit depth) can be found by integrating the velocity profile between StL1 (corresponding to y_1 and η_1) and the edge of the shear layer at the attachment point, given by

$$\dot{m}_{r1} = \rho \int_{y_1}^{y_{\text{ShL}}} u dy = \sqrt{\frac{3\zeta^2 \dot{m}^2 (R\theta + s_0)}{4b\sigma}} (\tanh(\eta_{\text{ShL}}) - \tanh(\eta_1)). \quad (24)$$

Note that the expressions for both \dot{m}_{e1} and \dot{m}_{r1} have been evaluated at $s = R\theta$. To clarify, StL1 refers to the whole streamline at $y = y_1$ and is not evaluated in s , while η_1 is defined at $s = R\theta$ and is given by $\eta_1 = y_1 \sigma / (R\theta + s_0)$.

H. Mass flows on the unattached side

A novel aspect of the present work is the modeling of the unattached side flows, which are shown in Fig. 8. The flow is shown to spread out across the entire channel some distance downstream of the

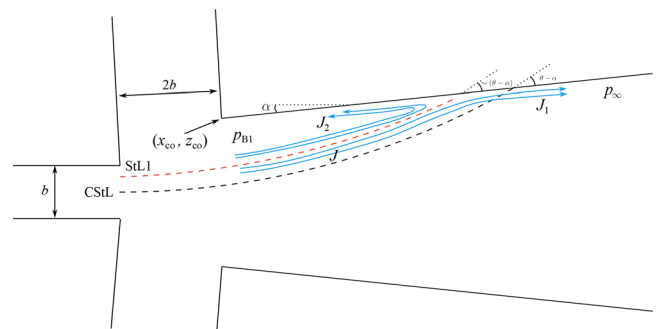


FIG. 7. Flow on the attached side around the attachment point. The streamline labeled “StL1” separates the flow that recirculates into the bubble from the flow that continues downstream. The central streamline is “CStL.”

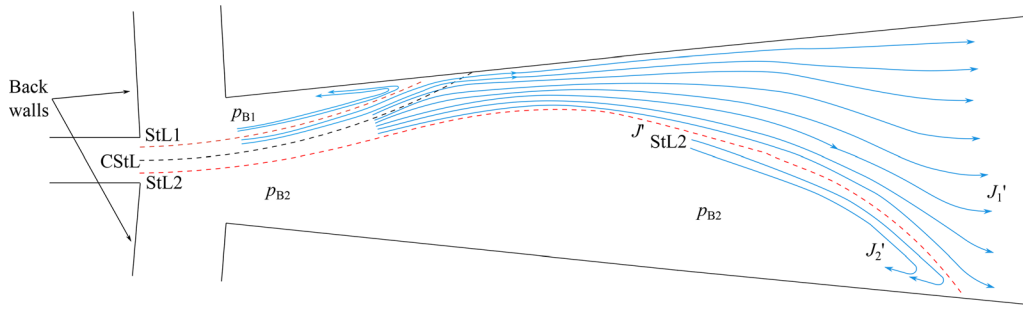


FIG. 8. Complete flow field, showing the flow dividing on the unattached side. “StL2” is streamline 2, which separates the flow that recirculates into the unattached side bubble from the flow that continues downstream.

attachment point. The channel has been assumed to be sufficiently long for this to occur before termination with an exit slot to atmospheric conditions. As such, forward flow must exist across the entire width of the exit slot, and an attachment point must exist on the unattached sidewall some distance downstream of the attached side attachment point, as shown in Fig. 8. The “attached side” is therefore the side to which the jet attaches first, after which it attaches to the “unattached side.” Streamline 2 (StL2) mirrors StL1 and separates flow that recirculates into the unattached side bubble from flow that continues downstream. The region in Fig. 8 on the unattached side between StL2 and the lower wall can be thought of as a recirculation bubble, although it is much larger and less well-defined than on the attached side. Its pressure, p_{B2} , is assumed to be uniform.

The entrainment and recirculation flows (per unit depth) on the unattached side are given by

$$\dot{m}_{e2} = \rho \int_{-\eta_{ShL}}^0 u dy - \frac{\dot{m}}{2} = \frac{\dot{m}}{2} \left(\sqrt{\frac{3\xi^2(x_{US} + s_0)}{b\sigma}} \tanh(\eta_{ShL}) - 1 \right), \quad (25)$$

$$\dot{m}_{r2} = \rho \int_{-\eta_{ShL}}^{-\eta_2} u dy = \frac{\dot{m}}{2} \sqrt{\frac{3\xi^2(x_{US} + s_0)}{b\sigma}} (\tanh(\eta_{ShL}) - \tanh(\eta_2)), \quad (26)$$

where $\eta_2 = y_2\sigma/(x_{US} + s_0)$ is the non-dimensional position of StL2 at $s = x_{US}$ in Fig. 8, and x_{US} is the length of StL2.

I. Momentum equation on the attached side

The control volume around the attachment point has a length L_1 perpendicular to the wall, as shown in Fig. 9. The momentum equation from the analysis of this control volume takes the form

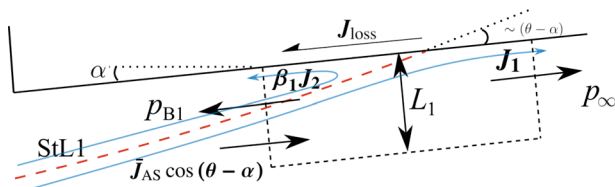


FIG. 9. Control volume on the attached side around the attachment point.

$$(p_{B1} - p_{\infty})L_1 = (J_1 - \beta_1 J_2) - \bar{J}_{AS} \cos(\theta - \alpha), \quad (27)$$

where p_{∞} is the pressure downstream of the control volume, J_2 is the momentum of the recirculation flow, J_1 is the momentum of the flow that continues downstream, and \bar{J}_{AS} is the fraction of the inlet momentum that enters the control volume. Since the bubble pressure is assumed to be uniform, the pressure at the upstream control volume edge must be the same as the mean pressure in the bubble. The local pressure rise at the attachment point is recovered from the dynamic head associated with the wall-normal component of the jet velocity as it stagnates against the wall. This static pressure is gradually converted to dynamic pressure over a distance upstream from the stagnation point. The momentum J_2 is associated with the dynamic head of this upstream flow if it were expanded isentropically to p_{∞} . The parameter β_1 describes the extent of the progress through the expansion process when the upstream boundary of the control volume is reached. This approach is required because the back wall of the channel (see Fig. 8) provides a physical obstruction to prevent the expansion from occurring in full. On the downstream side, $p_{\infty} = 0$ is taken, implying a downstream control volume edge far along the wall. Sawyer³⁷ measured the pressure along the attachment wall at several points, as well as along the wall in the spanwise direction. While the setback values used were larger than in the present work, the measured curves support the formulation of Eq. (27) and the use of β_1 .

The effect of acoustic excitation is to increase the entrainment rate on both sides of the jet, but more so on the side at which the excitation is directed.¹⁹ Figure 10 shows a series of sketches of the flow for the case where the pressure term is absent from the momentum conservation equation (27). The unexcited situation is shown in the top diagram in Fig. 10 (state A). When excited acoustically from the unattached side, the entrainment rate increases there more than on the attached side. This reduces the magnitude of the pressure difference across the jet, Δp , in Eq. (14), which causes θ to decrease and the attachment point to move downstream (state B). The behavior that follows depends on the form of the momentum equation. Taking the approach of Bourque and Newman²⁹ where the division of momentum depends only on the jet angle (known as the attachment point theory) means removing the pressure term from Eq. (27) and setting $\beta_1 = 1$. In this case, the only effect of the excitation on the momentum balance is that the jet strikes the wall at a less direct angle ($\theta - \alpha$ is smaller), so that less flow is recirculated. However, the excitation has caused the entrainment rate (per unit length) on the attached side to increase. Without a pressure term, a steady state can only be reached

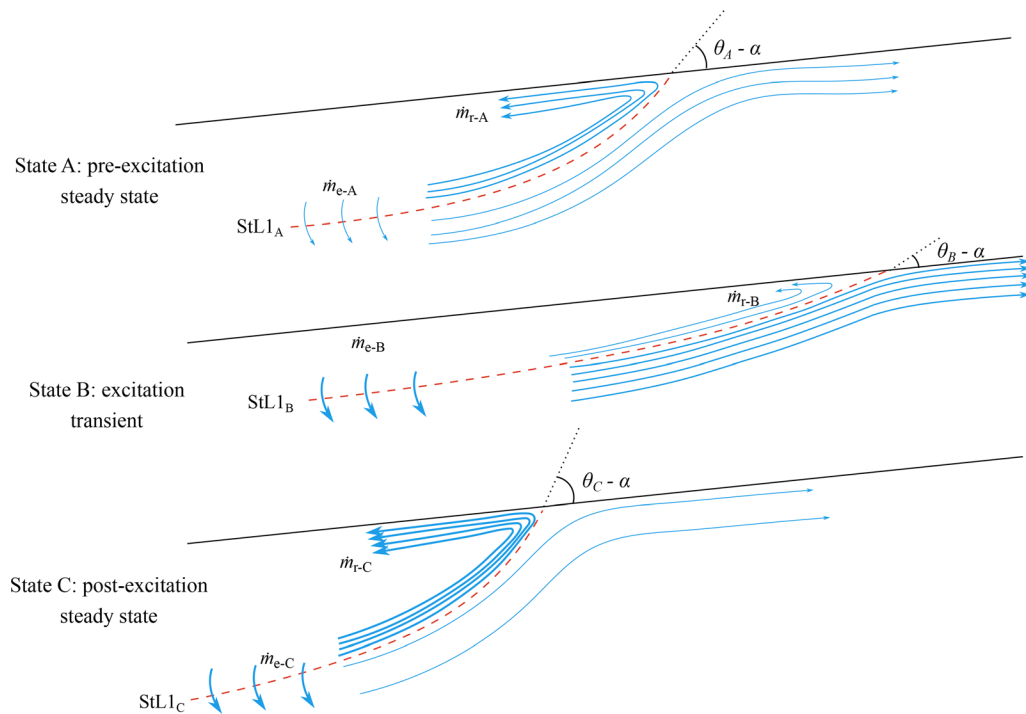


FIG. 10. Flow around the attachment point during the excitation transient if the pressure term is removed from the momentum conservation equation (27)—this is nonphysical behavior. The thickness and number of streamlines represent the quantity of mass flow.

when the jet strikes the wall at a more direct angle ($\theta - \alpha$ must increase) to supply the required increase in recirculation flow. The bubble pressure continues to drop until the absolute pressure difference across the jet is greater than it was before the excitation—the Coandă effect is strengthened (state C). This is the opposite of what is observed in reality, as demonstrated by Nicholls.⁵⁰

If instead (27) is used, the recirculation flow rate is able to increase to the new, acoustically excited rate of entrainment through the direct action of the stronger pressure gradient created by $p_{B1} - p_{\infty}$, and the Coandă effect is weakened, as expected. Numerous articles concerning reattaching jet models, both of the steady and unsteady varieties, have made use of the attachment point theory.^{29,35–41} The use of acoustic excitation has demonstrated this to be an over-simplification that leads to the incorrect conclusion.

J. Momentum equation on the unattached side

For the unattached side, a similar analysis uses a control volume with length L_2 perpendicular to the streamwise direction, taken around the attachment point on the opposite wall (Fig. 8). Analysis of the control volume gives the momentum equation

$$(p_{B2} - p_{\infty})L_2 = (J'_1 - \beta_2 J'_2) - \bar{J}_{US}, \quad (28)$$

where the variables mirror those on the attached side.

K. Momentum terms

The momentum terms are found by integrating the velocity profile with respect to y , giving

$$\begin{aligned} \bar{J}_{AS} &= \frac{3}{4} \left(t_{ShL} - \frac{1}{3} t_{ShL}^3 \right), \\ J_2 &= \frac{3}{4} \left(t_{ShL} - \frac{1}{3} t_{ShL}^3 - \left(t_1 - \frac{1}{3} t_1^3 \right) \right), \\ J_1 &= \frac{3}{4} \left(t_1 - \frac{1}{3} t_1^3 \right), \end{aligned} \quad (29)$$

where $t_{ShL} = \tanh(\eta_{ShL})$ and $t_1 = \tanh(\eta_1)$. On the unattached side, the terms are

$$\begin{aligned} \bar{J}_{US} &= \frac{3}{4} \left(t_{ShL} - \frac{1}{3} t_{ShL}^3 \right), \\ J'_2 &= \frac{3}{4} \left(t_{ShL} - \frac{1}{3} t_{ShL}^3 - \left(t_2 - \frac{1}{3} t_2^3 \right) \right), \\ J'_1 &= \frac{3}{4} \left(t_2 - \frac{1}{3} t_2^3 \right), \end{aligned} \quad (30)$$

where $t_2 = \tanh(\eta_2)$.

L. Radius of jet centerline

The jet radius, R , is related geometrically to the swept angle, θ , by

$$R = g(\theta) = \frac{z_{co} - x_{co} \tan(\alpha)}{1 - \cos(\theta) - \sin(\theta) \tan(\alpha)}, \quad (31)$$

where x_{co} and z_{co} are the positions of the corner between the sidewall and the control port relative to the center of the nozzle orifice (Fig. 7).

M. Nonlinear model

The preceding equations can be manipulated to produce a nonlinear model with states θ , $\dot{\theta}$, p_{B1} , and p_{B2} , given by solution of

$$\ddot{\theta} = \frac{\frac{1}{\rho}\Delta p + \frac{\bar{J}}{\rho g} - \zeta g' \dot{\theta} - \gamma g'' \dot{\theta}^2}{\gamma g'}, \quad (32)$$

$$\dot{p}_{B1} = \frac{c_3 \dot{m}}{2} \left[1 - \tanh\left(\frac{y_1 \sigma}{R\theta + s_0}\right) \sqrt{\frac{3\zeta^2(g\theta + s_0)}{b\sigma}} \right] f^{-1} - p_{B1} f' f^{-1} \dot{\theta}, \quad (33)$$

$$\begin{aligned} \dot{p}_{B2} = & \frac{c_3 \dot{m}}{2(V_{\text{const}} - f)} \left[1 - \tanh\left(\frac{y_2 \sigma}{x_{US} + s_0}\right) \sqrt{\frac{3\zeta^2(x_{US} + s_0)}{b\sigma}} \right] \\ & + \frac{p_{B2} f'}{(V_{\text{const}} - f)} \dot{\theta}, \end{aligned} \quad (34)$$

where $c_3 = R_0 T / M_m$ is a constant and $\tanh(y_1 \sigma / (R\theta + s_0)) = t_1$ is given by

$$\begin{aligned} -\frac{1}{4}(1 + \beta_1)t_1^3 + \frac{3}{4}(1 + \beta_1)t_1 - \frac{3}{4}\left(t_{\text{shL}} - \frac{1}{3}t_{\text{shL}}^3\right) \\ \times (\beta_1 + \cos(\theta - \alpha)) - \frac{p_{B1} L_1}{J} = 0, \end{aligned} \quad (35)$$

which results from manipulating the momentum equation on the attached side (27). Additionally, $\tanh(y_2 \sigma / (x_{US} + s_0)) = t_2$ is found from Eq. (28) and is given by

$$\begin{aligned} -\frac{1}{4}(1 + \beta_2)t_2^3 + \frac{3}{4}(1 + \beta_2)t_2 - \frac{3}{4}\left(t_{\text{shL}} - \frac{1}{3}t_{\text{shL}}^3\right)(\beta_2 + 1) \\ - \frac{p_{B2} L_2}{J} = 0. \end{aligned} \quad (36)$$

One potential weakness in the method used in the present work is that the coefficient of the damping term, ζ , in Eq. (14) is sensitive to the value of ν evaluated at $y = y_{\text{DSL}}$. A shape factor, κ , is therefore introduced on the \dot{R} term to ensure that the (assumed) jet velocity profile does not adversely affect the model.

N. Modeling the acoustic control input

It was explained in Sec. I that acoustically exciting a reattaching jet from the unattached side causes a biased increase in entrainment and spreading. The spreading is indicated by the parameter σ in the model. Up to this point, its value has been taken to be the same throughout. Different values of σ are introduced here for either side of the jet, σ_{AS} and σ_{US} , while the average of these values, σ_{mean} , is used in the evaluation of the jet curvature equation. This also results in three jet virtual origins because $s_0 = 0.46\sigma b$, leading to $s_{0,AS}$, $s_{0,US}$, and $s_{0,\text{mean}}$. In order to validate the model, the intention is to perturb the jet dynamically. As such, a time-varying input, σ_{\sim} , is added to the expressions for entrainment and recirculation on the unattached side only, to account for the bias in the effect of the excitation. This decision is discussed further in Sec. IV C.

III. MODEL ANALYSIS

A linearization approach was adopted for model analysis. This required operating points about which to linearize the dynamics,

which were found by solving for the system equilibrium at various conditions. The frequency responses of the linearized systems were calculated, and these provide the principal output of the model. A Monte Carlo method⁵¹ was used to evaluate the sensitivity of the frequency responses to uncertainties in the intrinsic model parameters. A single run of the Monte Carlo method works by drawing values for certain model parameters of interest from pre-determined probability distributions, solving for the system equilibrium, and computing the frequency response of the resulting linear model. This is repeated many times in order to produce an ensemble of frequency response curves. The standard deviation of this ensemble is indicative of the model sensitivity to the uncertainty in the parameters.

Parameter values were required to calculate operating points for linearization. Some parameters were fixed to correspond to a canonical fluidic device geometry, shown in Fig. 11, and are given in Table I. The setback and mass flow rate were varied independently of one another to form a “cross.” For each value of \dot{m} , the setback was fixed to $D = 2b$. For each value of D , \dot{m} was set to 5 g/s. The properties of the gas were changed to those of hydrogen, and the code was run at a different range of mass flow rates to keep the Mach number in the incompressible range, again at $D = 2b$. Hydrogen was chosen because it has a significantly different density to air. The linearization was conducted N_{MC} times at each $[D, \dot{m}, M_m]$ condition, where the molar mass, M_m , specifies the gas. The remaining parameters were chosen randomly for each linearization from a distribution of values as part of the Monte Carlo analysis, with the goal of assessing the model sensitivity to each parameter. Linearizing (32)–(34) leads to the state-space system

$$\dot{\mathbf{x}} = \mathbf{A}\mathbf{x} + \mathbf{B}u_{\text{in}}, \quad (37)$$

$$\mathbf{y} = \mathbf{C}\mathbf{x}, \quad (38)$$

where \mathbf{x} represents perturbations in the states $[\theta, \dot{\theta}, p_{B1}, \text{ and } p_{B2}]$ from their equilibrium positions, u_{in} is the control input ($u_{\text{in}} = \sigma_{\sim}$, since the equilibrium value of σ_{\sim} is 0), and y_{out} is the output of the system. Since the object of the model is to study the jet position dynamically, the output chosen is $y_{\text{out}} = \theta$, giving $\mathbf{C} = [1, 0, 0, 0]$. Taking Laplace transforms of Eqs. (37) and (38) and rearranging gives the single-input, single-output (SISO) transfer function

$$G(s) = \mathbf{C}(s\mathbf{I} - \mathbf{A})^{-1}\mathbf{B}. \quad (39)$$

A summary of the forms of the system in Eqs. (37)–(39) is given in the Appendix. To calculate this transfer function, the system equilibrium is required as an operating point at each flow rate, setback, and gas under consideration (Table I). Solving for the equilibrium of Eqs. (32)–(34) yields

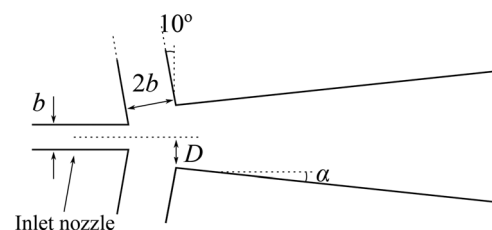


FIG. 11. Dimensions of geometry considered for model analysis.

TABLE I. Fixed parameters.

Parameter	b (mm)	d (b)	D (b)	α ($^\circ$)	x_0 (b)	y_0 (b)	\dot{m} (g/s)	Gas
Value	5	3	0.5–3	6	1.77	2	1–10, 0.2–2	Air, H ₂

$$-\Delta p = \frac{\bar{J}}{g}, \quad (40)$$

$$\tanh(\eta_1) \sqrt{\frac{3\xi^2(g\theta + s_0)}{b\sigma}} = 1, \quad (41)$$

$$\tanh(\eta_2) \sqrt{\frac{3\xi^2(x_{US} + s_0)}{b\sigma}} = 1. \quad (42)$$

The first equation (40) has reduced to the standard steady-state jet curvature equation. Equations (41) and (42) state that, on each side, the mass flow entrained into the jet must be equal to the flow recirculated from the jet in the steady state. Manipulation of Eqs. (41) and (42) reveals $\eta_1 = \eta_{DSL,AS}$ and $\eta_2 = \eta_{DSL,US}$, which means that the streamlines η_1 and η_2 are the dividing streamlines on either side of the jet in the steady state, as expected. Finally, Eqs. (35) and (36), which originated from momentum conservation equations, constrain the solution. Together, (40)–(42), (35), and (36) are algebraic equations that must be solved simultaneously to find the values of the states in the equilibrium. The unknown states and parameters are

$$\{\theta, p_{B1}, p_{B2}, \eta_1, \eta_2, \sigma_{AS}, \sigma_{US}, \kappa, x_{US}, V_{const}, \beta_1, \beta_2, L_1, L_2\}, \quad (43)$$

a total of 14 unknowns and 5 equations. The value of θ can be estimated from the literature. Bourque and Newman²⁹ and Sawyer³⁷ included data from which the radius of curvature can be calculated for several values of the setback, D . For these data, the wall incline angle was zero ($\alpha = 0$), but the value considered here is sufficiently small ($\alpha = 6^\circ$) to warrant use of their data as a guide, which are plotted in Fig. 12. The range of setback values used by Bourque and Newman²⁹

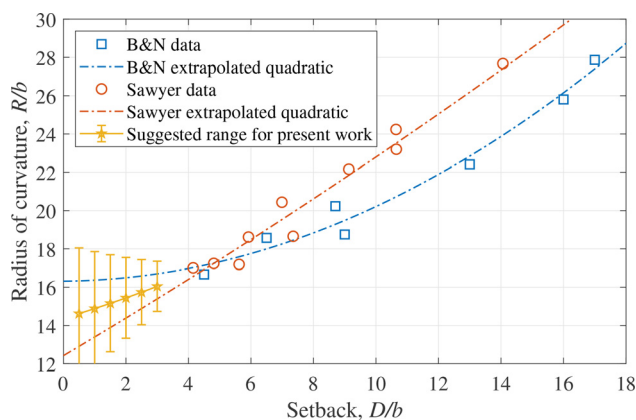


FIG. 12. Radius of curvature vs setback: data from Bourque and Newman²⁹ (blue squares) and fitted quadratic [$f_{B\&N}(D)$, dash-dot blue line], data from Sawyer³⁷ [$f_S(D)$, red circles] and fitted quadratic (dash-dot red line), and suggested ranges of values of R in the present work.

and Sawyer³⁷ exceeds the range of values in the present work ($0.5b \leq D \leq 3b$)—these were chosen because they capture most realistic fluidic device geometries—but extrapolation is possible. The figure also shows quadratic curves fitted to each dataset and the suggested range of values of R for the present work for each setback. The midpoint of each range is the mean of the two fitted curves, and the limits were set to double the distance from the midpoint to each curve, given by

$$f_S - \frac{1}{2}(f_{B\&N} - f_S) \leq R(D) \leq f_{B\&N} + \frac{1}{2}(f_{B\&N} - f_S), \quad (44)$$

where $f_{B\&N} = f_{B\&N}(D)$ and $f_S = f_S(D)$ are the quadratic curves fitted to the data from Bourque and Newman and Sawyer, respectively. The corresponding ranges of values of θ can be calculated from Eq. (31).

The volume nb^2d was not included in the Monte Carlo analysis because it is a geometric parameter that depends on the design of the control port. In the present work, the goal is to retain generality; hence, it was fixed to a value representative of a fluidic device, $n = 40$. It is shown in Sec. IV A 3 that the dynamics are relatively insensitive to n . The values of p_{B1} , p_{B2} , η_1 , η_2 , and L_1 are left to be determined by the solver. The remaining parameters were pre-tested to determine whether they should be included in the Monte Carlo analysis or set to a fixed value. The candidates for pre-testing are σ_{AS} , $\Delta\sigma = \sigma_{US} - \sigma_{AS}$, κ , x_{US} , V_{const} , β_1 , β_2 , and L_2 .

The spread factor on the unattached side, σ_{US} , should be lower than that on the attached side, σ_{AS} , because of both the naturally greater entrainment and the excitation (a lower σ indicates more spreading). The system is relatively insensitive to σ_{US} , and so, it was not included in the Monte Carlo analysis. In practice, the value is chosen to be 2 below σ_{AS} (whose value is discussed below), i.e., $\sigma_{US} = 5.7$.

The system is insensitive to x_{US} , and the only relevant lower bound is that it should far exceed the attached side entrainment length, i.e., $R\theta$. As such, its value is set to $x_{US} = 20b \approx 2R\theta$ and it was not included in the Monte Carlo analysis.

The value of β_2 does not significantly affect the shape of the frequency responses, but $\beta_2 > 0.1$ causes a small proportion of the Monte Carlo runs to produce unstable systems. Unstable behavior is nonphysical and is a product of an invalid combination of parameters. Since perturbing β_2 around this value does not produce a noticeable difference, it is fixed at $\beta_2 = 0.1$ and was not included in the Monte Carlo analysis.

The remaining parameters were included in the Monte Carlo analysis. The ranges for these parameters, and for the swept angle, θ , are discussed here.

A. Swept angle, θ

The swept angle was initially limited to correspond to the ranges of R in Eq. (44). However, this resulted in a number of unstable systems. It is possible to identify the parameter values that caused instability by comparing the mean value of each parameter across every

system with the mean value from the subset of the unstable systems. This indicated that the lower bound of R should be increased, so that the range for R used was

$$f_s + (1/10)(f_{B\&N} - f_s) \leq R(D) \leq f_{B\&N} + \frac{1}{2}(f_{B\&N} - f_s), \quad (45)$$

and the corresponding θ ranges were found from Eq. (31).

B. Attached side spread factor, σ_{AS}

The nominal value of the attached side spread factor, σ_{AS} , is the free jet value, $\sigma_{AS} = 7.7$.³³ The fact that the jet is curved and attached causes less entrainment on the attached side of the jet,³² which would imply that $\sigma_{AS} > 7.7$. However, the increased entrainment due to the acoustic excitation decreases the value of σ_{AS} , so it is left as the free jet value. There was no obvious means of determining a range for the value of σ_{AS} . It has a considerable effect on the system responses, mostly on the damping. The range selected was the nominal value $\pm 20\%$, giving

$$6.16 \leq \sigma_{AS} \leq 9.24. \quad (46)$$

C. Shared bubble volume, V_{const}

The nominal value of the volume shared by the bubbles on each side, V_{const} , is set to $500b^2d$. The total channel volume in the geometry considered is $\sim 1000b^2d$, but the jet is likely to take up a large portion of this volume, so the upper bound for the range is set as $750b^2d$. The effect of varying V_{const} is to modify a real pole in $G(s)$ associated with the unattached side bubble pressure dynamics independently of the others. When it is increased, the pole approaches the origin, and its roll-off becomes more important. The limits chosen were those of the physically reasonable range for the geometry, given by

$$250 \leq \frac{V_{\text{const}}}{b^2d} \leq 750. \quad (47)$$

D. Fraction of attached side recirculated momentum, β_1

The parameter β_1 can take values between 0 and 1. The nominal value of β_1 was set to the midpoint of these limits. The value of β_1 is significant in determining the value of L_1 , the attached side control volume length that is set by the solver. Spatial constraints limit the range of physically reasonable values of L_1 to be $0 \leq L_1 \leq D$. When $\beta_1 > 0.7$, the operating point is solved to give $L_1 > D$, and, incidentally, unstable systems are produced. Similarly, when $\beta_1 < 0.35$, unstable systems are produced in some conditions. The range for β_1 was therefore limited to

$$0.35 \leq \beta_1 \leq 0.7. \quad (48)$$

E. Shape factor, κ

The shape factor scales the transverse velocity at the dividing streamlines on either side of the jet. Its range was initially set to $1/5 \leq \kappa \leq 5$, but values of $\kappa < 2.2$ were found to produce unstable systems. Its range was therefore bounded to

$$2.2 \leq \kappa \leq 5. \quad (49)$$

F. Unattached side control volume length, L_2

The physically reasonable range of L_2 was taken as $0 \leq L_2 \leq 3D$, again as a result of spatial constraints. Values of $L_2 < 1.5D$ result in unstable systems, so the range for L_2 was set to

$$1.5D \leq L_2 \leq 3D. \quad (50)$$

The parameter ranges are summarized in Table II, along with the parameters that were not included in the Monte Carlo analysis. Truncated normal probability density functions for each parameter range were used to produce random values for the Monte Carlo analysis. The distributions were truncated at the limits in Table II and were scaled so that these limits coincided with two standard deviations from the mean. The number of values taken was $N_{MC} = 200$, and the equilibrium and linearization were computed for each value. The mean and standard deviation of the resulting model magnitude and phase responses were computed at each frequency. These frequency responses are shown in Fig. 13, where the shaded area represents one standard deviation from the mean. The mean response for each flow rate is shown for a comparative view in Fig. 14. The roll-off frequency, defined as the -3 dB point in the magnitude response, is shown against flow rate in Fig. 15(a). To determine the sensitivity of the roll-off frequency with respect to the setback, the Monte Carlo analysis was run at 5 g/s with D taking values from $D = 0.5b$ to $D = 3b$. The data are shown in Fig. 15(b). Unfortunately, it was not possible to investigate varying the wall incline angle, α , because the steady-state radius of curvature depends on α and D .^{29,37} No data for the radius of curvature with varying values of α were available in the literature. In perturbing α , it would not be possible to distinguish the model sensitivity from the error in the operating point for linearization (the value of R). To distinguish between the model dependence on mass flow rate and velocity, the gas properties were changed to those of hydrogen. The hydrogen mass flow rates were chosen to match the air velocities using the density ratio, which is equal to the ratio of the specific gas constants for incompressible flows. Figure 16 shows the roll-off frequency against jet velocity for both air and hydrogen. The velocity where $M_{\text{air}} = 0.3$ is highlighted to respect the fact that higher velocities stretch the assumption of incompressibility used in the model. The Mach numbers for hydrogen in Fig. 16 are not close to the limit of incompressibility.

Figure 17 shows the linearized system responses to a step change in the input, σ_{∞} , at several flow rates. The y axis is the system output,

TABLE II. Ranges for parameters varied in the Monte Carlo analysis and fixed values for those excluded.

Parameter	θ	σ_{AS}	V_{const}	β_1	κ	L_2
Range	See Eq. (45)	6.16–9.24	250–750 b^2d	0.35–0.7	2.2–5	1.5–3D
Parameter	σ_{US}	x_{US}	β_2	n		
Value	$\sigma_{AS} - 2$	$20b$	0.1	40		

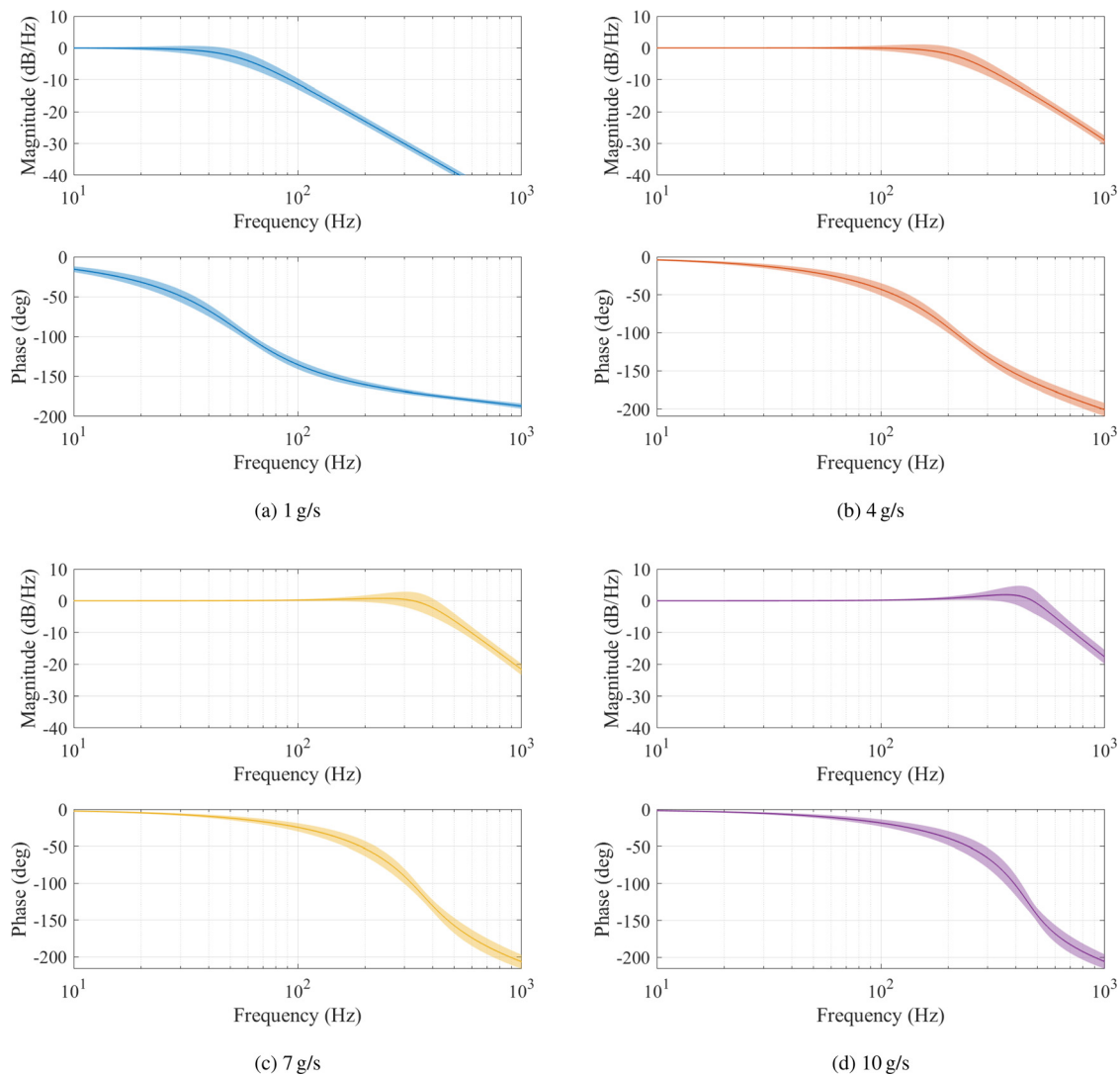


FIG. 13. Model frequency responses: mean (solid line) and one standard deviation from mean (shaded area) from the Monte Carlo analysis ($N_{MC} = 200$) at several flow rates (air).

$y_{out} = x_1$, which is the deviation in θ from the operating point. Note that the values have been normalized to unity because the DC gain—the ratio of the change in the steady-state value of x_1 relative to the size of the step input—is not modeled. The nominal parameters were used to generate these linearized systems (the mean value of the range for each parameter in Table II), using air. A more physical interpretation of Fig. 17 is that it shows how the jet position responds transiently to a step change in the amplitude of the acoustic excitation (for example, switching the excitation on).

IV. DISCUSSION

A. Modeling approach

1. Görtler profile

The Görtler profile is for a free rather than an attached jet. By the time particles have traveled to the attachment point, their velocities

must have resolved into the wall-parallel direction. Additionally, the jet is confined on the attached side and there is a recirculation bubble adjacent to it. Sawyer³⁷ calculated the Görtler profile projection onto the direction parallel to the wall at two stations with $\sigma = 15$ and set the profile momentum using measurements with pitot-static tubes. The calculated profiles showed no sign of asymmetry and were demonstrated to agree closely with scaled plane jet measurements made by Forthmann,⁵² albeit for larger values of setback than in the present work. While the smaller setbacks used in this paper could affect the profile, the available evidence justifies use of the Görtler profile in this case.

The starting point of the derivation of the Görtler profile is Prandtl's assumption that the eddy viscosity is proportional to jet width and centerline velocity at a given downstream station.³¹ The concept of eddy viscosity derives from the Boussinesq hypothesis, and its application implies isotropic turbulence.⁵³ The jet potential core is

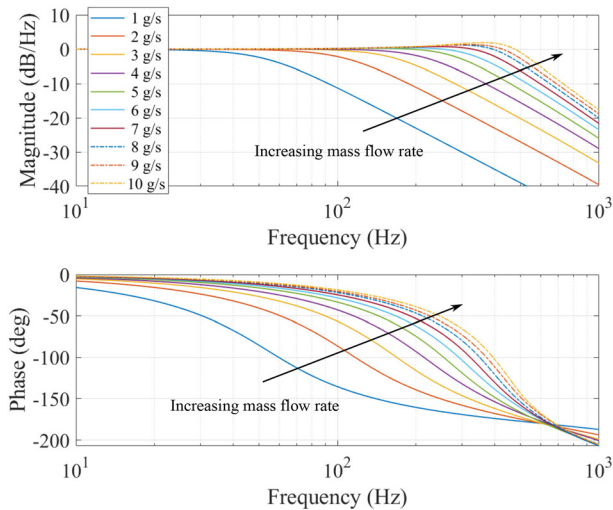
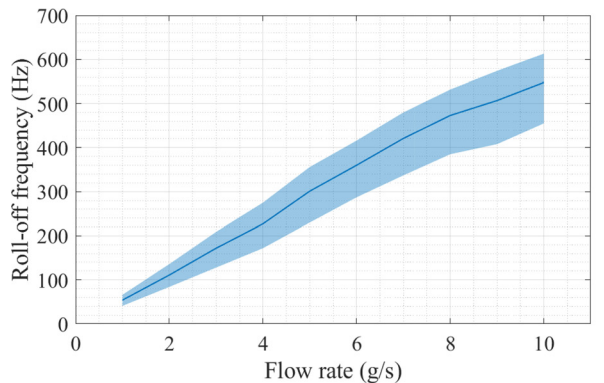
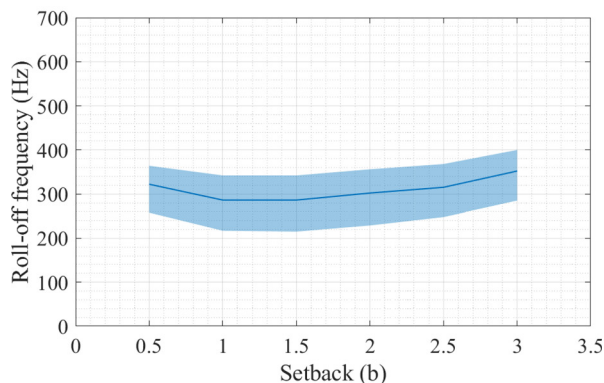


FIG. 14. Model frequency responses (mean from the Monte Carlo analysis ensemble) at several flow rates (air).



(a) Roll-off frequency vs flow rate ($D = 2b$)



(b) Roll-off frequency vs setback ($\dot{m} = 5 \text{ g/s}$)

FIG. 15. Model roll-off frequency vs flow rate (a) and vs setback (b), determined by -3 dB point in magnitude response (air).

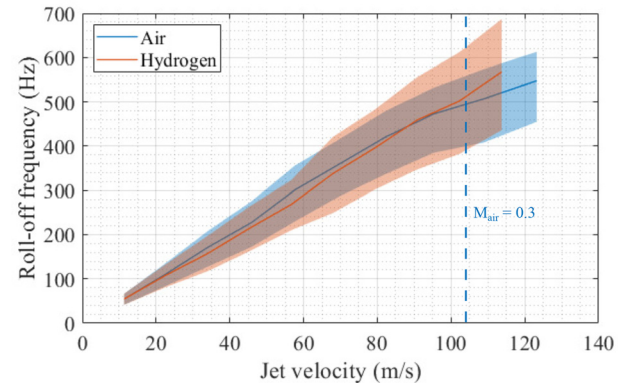


FIG. 16. Roll-off frequency vs jet velocity, air (blue) and hydrogen (red), with line showing $M_{\text{air}} = 0.3$ (dashed blue).

typically around three to five inlet nozzle diameters in length, depending on the excitation provided.¹¹ The turbulence cannot be considered isotropic for stations upstream of the end of the potential core; indeed, vortices persist beyond the potential core for some distance. The strategy adopted in this paper has been to match the Görtler profile to the nozzle exit conditions by a continuity argument.

An improvement might be to characterize the velocity profile experimentally at several stations downstream of the nozzle orifice to determine the station where it becomes possible to match the Görtler profile. This was the approach taken by Sawyer,³² but as explained in Sec. I, the added complexity of using an experimentally validated velocity profile was deemed to outweigh the improvement in accuracy. Sawyer's³² approach would preclude the analytical approach that follows, as well as the linearization used to analyze the model. Here, the goal has been to capture the important dynamics with the simplest possible description of the system. An experimental validation of the velocity profile using particle image velocimetry (PIV) is described in a separate paper. Our results demonstrate that the residual error from fitting the Görtler profile decays by around 3 nozzle widths downstream of the orifice and that the profile asymmetry is small.

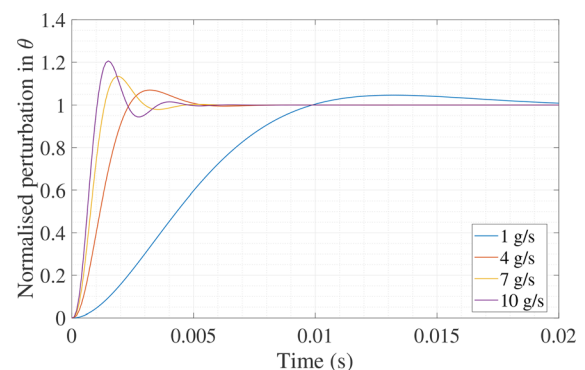


FIG. 17. Linearized system step response: normalized x_1 (deviation in θ from operating point) in response to step change in σ_w .

2. Jet curvature equation

Kirshner and Katz⁴² suggested that the quasi-steady jet assumption widely used in the literature typically represents the weakest component of each model.^{35,36,39–41} Lush³⁵ and Chang³⁹ used a scaling argument to show that an inertial term in the Cartesian Navier–Stokes streamwise momentum equation dominated the unsteady term if the transport time of particles through a fluidic device is significantly less than the switching time. However, it was from the inertial term that the unsteady damping term (in \dot{R}) in the jet curvature equation originated. Furthermore, since these studies used the quasi-steady jet curvature equation during the switching phase where the jet was still attached, the appropriate scale for comparison with the transport time is the attached jet response time, which is typically much smaller than the overall switching time.⁴¹ Calculations based on the roll-off frequency of the model responses in Nicholls and Bacic²⁷ indicate that the jet response time is comparable to the transport time. The jet curvature equation derived in this paper removes the need for the quasi-steady jet assumption by modeling the bulk jet dynamics.

3. Bubble pressure model

The dynamic pressure associated with the swirling flow in the bubble was assumed to be negligible. The elongated shape of the bubble due to the small setback limits the maximum size of vortex that can form in the bubble and hence limits the radial pressure gradient caused by the circulating flow. Sawyer³⁷ made measurements that showed that the spatial variation in pressure reduced with setback. The static pressure varied spatially by a factor of approximately 1.25 from the mean value with the smallest setback used ($D = 4.16b$), which is more than double the nominal setback in the present work ($D = 2b$). This justifies the exclusion of the dynamic pressure due to the swirling flow.

The volume of the control port, nb^2d , was excluded from the Monte Carlo analysis, as explained in Sec. III. Nevertheless, the model has some dependence on its value. The value of n principally affects the system damping—that is, the size of the resonant peak in the frequency response, which determines the amount of overshoot in the response to a step input in the time domain. As an illustration of the sensitivity of the dynamics to this parameter, the value of n was doubled (to $n = 80$) and the model was re-run at a middling condition ($\dot{m} = 5$ g/s, $D = 2b$, air). The roll-off frequency increased by 4% and the damping ratio decreased by 10%.

4. Aspect ratio

The flow has been assumed to be 2D in the present work. However, in certain applications of fluidic devices, spatial constraints drive the device aspect ratio (AR) to relatively small values where the 2D assumption is invalid. For example, Müller³⁴ described how the end walls reduce turbulence production in the jet, thereby reducing the entrainment rate. This means that a lower aspect ratio results in an equilibrium state of the jet with weaker attachment—the radius of curvature is larger. Similarly, Epstein⁴¹ suggested that σ , the inverse of the entrainment rate, must depend on AR. One possible means of incorporating the 3D effects into the model could be to characterize experimentally the radius of curvature, R , with respect to AR in addition to the 2D parameters (setback, D , and wall incline angle, α). This

characterization could be used to choose a more appropriate value of R for the operating point for model linearization.

B. Discussion of model results

The frequency responses shown in Figs. 13 and 14 describe the dynamics of how the jet curvature (and therefore position) responds to acoustic perturbations. The roll-off frequency of each curve is indicative of the temporal response, and a first approximation of the system response time to a step input is given by the inverse of the roll-off frequency.

The motivation for the Monte Carlo analysis is that the values of many of these intrinsic model parameters are unknown. It was possible to bound the parameters in Sec. III through use of physical reasoning and by ruling out parameter ranges that resulted in unstable linearized systems (since all experimental evidence suggests that the reattaching jet dynamics are stable). The Monte Carlo analysis allows an assessment to be made of how these parameter uncertainties propagate through to the model frequency response curves in Fig. 13 and the corresponding sensitivity region in Figs. 15 and 16.

Figure 15(b) reveals that there is a relatively weak dependence of the roll-off frequency on setback distance, D . The exclusion of the dynamic pressure from the bubble pressure model discussed in Sec. IV A 3 may mean that Fig. 15(b) underestimates the dependence of the roll-off frequency on setback for significantly larger values of D .

It was demonstrated in Fig. 15(a) that the roll-off frequency displays a linear dependence on flow rate. Since the Mach numbers were kept within the incompressible regime, the density is approximately constant in Fig. 15(a), and it is not possible to distinguish between mass flow rate and velocity dependence. Changing the gas properties to those of hydrogen, and setting the mass flow rate to match the air case, produced the results shown in Fig. 16. This figure shows the roll-off frequency for air and hydrogen against jet velocity, and demonstrates velocity, rather than mass flow rate, dependence.

The velocity dependence can be explained by the consideration of the model equations and the poles and zeros in the linearized system. The poles and zeros are plotted in Fig. 18 for the mean values of each parameter range in Table II, $D = 2b$, and gas properties appropriate to air at several values of \dot{m} . The figure demonstrates that for most flow rates, a complex conjugate pair of poles dominates the system. At the highest flow rate, a real pole starts to become significant, although the

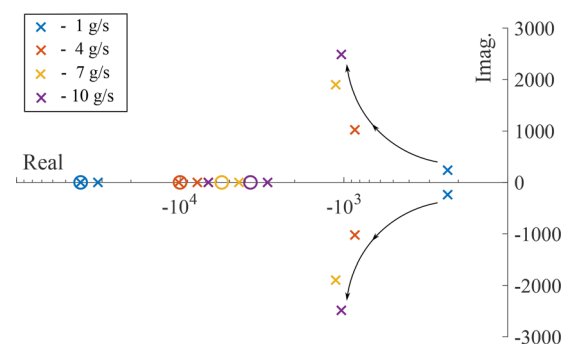


FIG. 18. Poles (crosses) and zeros (circles) of the linearized system for the mean parameter values at several flow rates (air). Real axis on a log scale, arrows show the progression of complex conjugate pole pair with increasing flow rate.

nearby zero reduces its effect. This explains the reducing gradient in Fig. 15(a) at higher flow rates—the real pole lowers the bandwidth. However, for most flow rates, the complex pair is most significant for the system frequency response. To investigate the link between the nonlinear equations (32)–(34) and the poles and zeros, the equations were perturbed before linearization. This involved applying a fictitious gain in each equation in turn and observing the movement of the poles and zeros. This exercise demonstrated that each real pole depends most strongly on the bubble pressure equations (33) and (34), respectively. The complex conjugate pair was revealed to depend most strongly on the jet curvature equation (32). Taking the jet curvature, Eq. (14), and setting the forcing function to zero ($\Delta p/\rho = 0$) give

$$\gamma \frac{d^2 R}{dt^2} + \zeta \frac{dR}{dt} - \frac{\bar{J}}{\rho R} = 0. \quad (51)$$

The density appears in the $1/R$ term in Eq. (51) as $\bar{J}/\rho \approx \rho \bar{u}^2 b/\rho = \bar{u}^2 b$, where \bar{u} is the mean nozzle velocity. Inspection of the coefficients γ and ζ in Eqs. (13) and (15) reveals their independence of density as well. The acceleration coefficient, $\gamma = 2\gamma_{\text{DSL}}$, depends on the dividing streamline position, which is given by Eq. (7) and is independent of both \bar{u} and ρ . The damping coefficient, ζ , depends on the transverse velocity evaluated at the dividing streamline, which depends on the mean nozzle velocity. Upon linearization, (51) takes the form of the standard, unforced, second-order linear system

$$\ddot{y} + 2\zeta'\omega_0\dot{y} + \omega_0^2 y = 0, \quad (52)$$

where ζ' is the damping ratio and ω_0 is the natural frequency. The roll-off frequency of the system in Eq. (52) is determined predominantly by ω_0 . The equivalent coefficient in Eq. (51) was shown above to be $\bar{J}/\rho \approx \bar{u}^2 b$. Comparing these coefficients explains the linear dependence of the system response on the jet velocity observed in Fig. 16.

The link between the jet curvature equation and the complex conjugate poles that dominate the linearized system implies that it is the response of the jet, rather than that of the recirculation bubbles, that dominates the dynamics. In the context of a temporal step response (Fig. 17), this means that the bubble pressures respond to the acoustic input much more quickly than the jet responds to the changing bubble pressures. This underlines the importance of modeling the bulk jet dynamics as in Eq. (51).

C. Effect of excitation on attached side spreading

It has been explained that while the acoustic excitation increases the entrainment on both sides of the jet, the effect is greater on the unattached side. As such, the acoustic input was assumed only to affect the unattached side spread factor, which became $\sigma_{\text{US}} + \sigma_{\sim}$. When first tested, including σ_{\sim} on the attached side had a negligible effect on the system dynamics. However, more detailed analysis has shown that the dynamics are insensitive to fractions of σ_{\sim} appearing in the attached side ideal gas law (33) up to a limit, at which point there is a reversal of the jet response to acoustic excitation. In other words, above this limit, excitation strengthens rather than weakens the jet attachment.

The effect of including a fraction of the system input, σ_{\sim} , in the attached side ideal gas law (33) depends on the quantity included. In this discussion, the fraction included is ϵ , so that σ_{AS} is replaced with $\sigma_{\text{AS}} + \epsilon\sigma_{\sim}$. Reference to Fig. 8 may aid comprehension of the

following discussion. When a constant acoustic excitation tone (no amplitude modulation) is switched on, the unattached side bubble pressure reduces because there is a net entrainment of flow into the jet in the transient. At the unattached side attachment point, a greater portion of the jet is sucked upstream by the reducing pressure. This increasing recirculation flow rate acts as a negative feedback to settle the unattached side bubble pressure. The pressure reduction decreases the magnitude of the pressure difference across the jet, which causes the attached side attachment point to move downstream and the radius of curvature to increase. On the attached side, even with $\epsilon = 0$ (which has been assumed up to this point), there are three things that cause the bubble pressure to decrease. First, the larger value of R results in a longer entrainment length, so that even with an unchanged attached side spread factor (which defines the entrainment per unit length rather than the total entrainment flow rate), the entrainment flow rate increases. Second, the weaker attachment means that the jet strikes the wall at a less direct angle, which reduces the recirculation flow rate. The imbalanced entrainment and recirculation flow rates cause a net mass flow rate leaving the bubble, which reduces its pressure. Finally, the increased radius of curvature increases the bubble volume, which also reduces its pressure. At the attached side attachment point, more flow is sucked upstream by the reduced bubble pressure. This increased recirculation flow rate stabilizes the bubble pressure and a steady state is reached when the recirculation flow rate increases to the larger entrainment flow rate.

The only difference to this chain of events when $\epsilon > 0$ is that the attached side entrainment flow rate increases directly under the action of the excitation. The increased entrainment on each side of the jet reduces the pressure on each side—the resulting difference, Δp , determines the change in attachment strength. The net change in Δp therefore depends on the effectiveness with which the change in entrainment can reduce the pressure. This effectiveness is determined by the entrainment length and by the impact of the resulting pressure reduction on the recirculation flow rate via the momentum balance on each side. These effects act against each other—the entrainment length on the unattached side is double the typical value on the attached side, but the larger value of L_2 (the control volume length along which p_{B2} acts to draw flow into the unattached side bubble) compared with L_1 (the same on the attached side) means the recirculation mechanism is more effective on the unattached side. With the parameter values used in this paper, this stronger recirculation mechanism (inhibits bubble pressure reduction) outweighs the direct increase in entrainment length (drives bubble pressure reduction). Therefore, setting an even sensitivity to excitation on both sides of the jet ($\epsilon = 1$) means that excitation causes a larger reduction in bubble pressure on the attached side than the unattached side, so that the magnitude of the pressure difference across the jet is increased. The result is that excitation strengthens rather than weakens attachment. This is not observed in reality.

It is possible to bound the value of ϵ to be less than the critical value, ϵ_0 , where the steady state under the impact of excitation has no net effect on attachment strength. This value is $\epsilon_0 = 0.245$, which is independent of flow rate. Increasing ϵ decreases the system DC gain (the steady state change in θ resulting from a given value of σ_{\sim}) until the critical value, ϵ_0 , where the DC gain passes through 0. The bound $\epsilon < \epsilon_0$, therefore, limits the model to the observed behavior of weakening, rather than strengthening, the attachment. The goal of the model presented in this paper has been to describe the system frequency

response; it has not attempted to predict the DC gain. Bounding $\epsilon < \epsilon_0$ is a relatively conservative limit. However, it is possible to place a stricter bound on ϵ by considering the effect of its value on the system zero in $G(s)$. As ϵ increases, the zero approaches $-\infty$ at some limiting value, ϵ_1 ($\epsilon_1 < \epsilon_0$). When ϵ increases beyond ϵ_1 , the zero re-appears at $+\infty$, then moves toward the origin, reaching its critical value (ϵ_0) when it arrives at $(0, 0)$. In the range $\epsilon_1 < \epsilon < \epsilon_0$, the zero is on the positive real axis, which means the system is non-minimum phase. This variety of linear systems has a characteristic feature in its transient step response, which is that the system output (θ in this case) “goes the wrong way” initially, before reaching its steady state. For example, the step response of a non-minimum phase system with a positive DC gain would initially become negative in the transient, before increasing above the axis and settling to a positive steady value. The duration and magnitude of the inversion depends on the position of the zero—the closer to the origin, the more dominant and obvious the inversion. The step response to excitation in the experiment suffers from a weak signal-to-noise ratio, and while this can be improved with many repeats and temporal averaging, it is not possible to exclude the possibility of a very small inversion in the response. However, a probable bound that can be placed on ϵ is ϵ_1 , the limiting value beyond which the system becomes non-minimum phase, which takes the value $\epsilon_1 = 0.193$ and is invariant to flow rate.

The value of ϵ_1 is independent of the fraction of recirculated momentum exiting the upstream boundary of the control volumes on either side of the jet, β_1 and β_2 , and insensitive to the unattached side entrainment length, x_{US} . It does depend on the volume that the attached and unattached side bubbles share, V_{const} . Conversely, ϵ_0 is independent of V_{const} , insensitive to β_1 and β_2 , but depends on x_{US} . The culmination of these dependencies is that the bound on ϵ is robust to the particular model parameters used. While ϵ was not included in the Monte Carlo analysis, its effect on the frequency response is negligible until its value is close to ϵ_0 .

V. SUMMARY AND CONCLUSIONS

This paper has detailed the development of an analytical model that describes the dynamics of a reattaching jet, the core of a fluidic device. A novel, unsteady jet curvature equation was derived from first principles, which provided the central element of the model. Several equations were derived and combined with the jet curvature equation to form the model. This consisted of a set of nonlinear differential equations (32)–(34) with associated algebraic constraints (35) and (36). Another novel aspect was the modeling of an acoustic input as a varying spread factor. The nonlinear equations were linearized using data from the literature to provide operating points, producing a fourth-order state-space system. A Monte Carlo analysis was conducted to determine the model sensitivity to certain unknown parameters. The parameter ranges for the probability distributions were refined to maintain stability of the linearized system in every run of the analysis. The Monte Carlo analysis was repeated at several mass flow rates for both air and hydrogen, and a range of setback values using air. The roll-off frequency of the Bode plot of the linearized system was used to characterize the model. The trends revealed a weak dependence on the setback and a linear dependence on the jet velocity. The latter was explained through the additional analysis of the linearized system poles and zeros and of the jet curvature equation. The influence of the excitation on the attached side was investigated. The increase in spreading on the attached side relative to the unattached

side was bounded by consideration of its effect on the resulting model behavior. This bound was shown to be robust to flow rate, as well as uncertain intrinsic model parameters.

We have argued that the justification for using the quasi-steady jet assumption is weak in the context of attached jet dynamics. The unsteady jet curvature equation removes the need for this assumption. An alternative approach to setting the jet virtual origin, when combined with an inflated Görtler velocity profile, resulted in a well-behaved dividing streamline that coincides with the edge of the nozzle. The boundary of the model domain was defined by the consideration of the transverse velocity profile, which indicated that there is no contribution to the jet from beyond the edge of the shear layer. Bourque and Newman’s widely used “attachment point theory” approach to momentum resolution yielded a jet response to acoustic excitation that is the opposite of what is observed in practice. This motivated the development of an alternative momentum equation that correctly predicts the response of the jet to be a decrease in attachment strength.

The core element of most fluidic devices is the reattaching jet. The model developed in this paper describes quantitatively a reattaching jet’s dynamical behavior and will therefore facilitate the design and control of fluidic devices. A separate paper describes the experimental validation of the model presented here. In this paper, an assessment is made of the model assumptions, and the jet frequency response to acoustic excitation is determined experimentally for comparison with the model output in Fig. 13.

ACKNOWLEDGMENTS

The authors gratefully acknowledge the support of the ATI grant Powerplant Integration of Novel Engine Systems (PINES), UKRI Project Reference No. 113263 (<https://gtr.ukri.org/projects?ref=113263>).

AUTHOR DECLARATIONS

Conflict of Interest

The authors have no conflicts to disclose.

Author Contributions

Chris James Nicholls: Conceptualization (lead); Formal analysis (lead); Investigation (lead); Methodology (lead); Writing – original draft (lead). **Brian Ming Tak Tang:** Formal analysis (supporting); Methodology (supporting); Supervision (equal); Writing – original draft (supporting). **James Turner:** Formal analysis (supporting). **Marko Bacic:** Formal analysis (supporting); Funding acquisition (lead); Methodology (supporting); Supervision (lead); Writing – original draft (supporting).

DATA AVAILABILITY

The data that support the findings of this study are available from the corresponding author upon reasonable request.

APPENDIX: LINEARIZATION, STATE-SPACE, AND TRANSFER FUNCTION

The nonlinear system to be linearized is defined by

$$\frac{d}{dt} \begin{bmatrix} x_1 \\ x_2 \\ x_3 \\ x_4 \end{bmatrix} = \begin{bmatrix} f_1(\mathbf{x}, u_{in}) \\ f_2(\mathbf{x}, u_{in}) \\ f_3(\mathbf{x}, u_{in}) \\ f_4(\mathbf{x}, u_{in}) \end{bmatrix}, \quad (\text{A1})$$

where $[x_1, x_2, x_3, x_4]$ are the perturbations of the states $[\theta, \dot{\theta}, p_{B1}, p_{B2}]$ about the operating point, $u_{in} = \sigma_{\sim}$, and the functions f_1 to f_4 are defined by Eqs. (32)–(36). The linearized system is given by

$$\dot{\mathbf{x}} = \mathbf{A}\mathbf{x} + \mathbf{B}u_{in}, \quad (\text{A2})$$

$$y_{out} = \mathbf{C}\mathbf{x}, \quad (\text{A3})$$

where

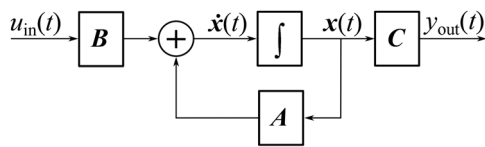
$$\mathbf{A} = \begin{bmatrix} \frac{\partial f_1}{\partial x_1} & \frac{\partial f_1}{\partial x_2} & \frac{\partial f_1}{\partial x_3} & \frac{\partial f_1}{\partial x_4} \\ \frac{\partial f_2}{\partial x_1} & \frac{\partial f_2}{\partial x_2} & \frac{\partial f_2}{\partial x_3} & \frac{\partial f_2}{\partial x_4} \\ \frac{\partial f_3}{\partial x_1} & \frac{\partial f_3}{\partial x_2} & \frac{\partial f_3}{\partial x_3} & \frac{\partial f_3}{\partial x_4} \\ \frac{\partial f_4}{\partial x_1} & \frac{\partial f_4}{\partial x_2} & \frac{\partial f_4}{\partial x_3} & \frac{\partial f_4}{\partial x_4} \end{bmatrix}_{\text{o.p.}}, \quad \mathbf{B} = \begin{bmatrix} \frac{\partial f_1}{\partial u_{in}} \\ \frac{\partial f_2}{\partial u_{in}} \\ \frac{\partial f_3}{\partial u_{in}} \\ \frac{\partial f_4}{\partial u_{in}} \end{bmatrix}_{\text{o.p.}}, \quad (\text{A4})$$

$$\mathbf{C} = [1 \ 0 \ 0 \ 0], \quad (\text{A5})$$

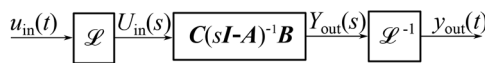
where o.p. refers to the evaluation of the terms at the operating point [the equilibrium that is given by the solution of Eqs. (40)–(42)], and \mathbf{C} was chosen to select the output as $x_1 = \theta$, the swept angle. Taking Laplace transforms and manipulating (A2) and (A3) leads to the input–output relationship

$$G(s) = \mathbf{C}(s\mathbf{I} - \mathbf{A})^{-1}\mathbf{B}. \quad (\text{A6})$$

The two forms of the system are shown diagrammatically in Fig. 19. To evaluate the magnitude and phase responses shown in Figs. 13 and 14, $s = j\omega$ was substituted into the expression for $G(s)$ in Eq. (A6).



(a) State-space system model



(b) Transfer function model

FIG. 19. Forms of linear models used in the present work.

REFERENCES

- ¹B. Steinfurth, F. Haucke, and J. Weiss, "Assessment of two fluidic actuators for active flow control on a one-sided diffuser," *CEAS Aeronaut. J.* **10**, 633–643 (2019).
- ²M. A. Hossain, R. Prenter, R. K. Lundgreen, A. Ameri, J. W. Gregory, and J. P. Bons, "Experimental and numerical investigation of sweeping jet film cooling," *J. Turbomach.* **140**, 031009 (2018).
- ³M. DeSalvo, E. Whalen, and A. Glezer, "High-lift enhancement using fluidic actuation," AIAA Paper No. 2010-863, 2010.
- ⁴G. Raman and S. Raghu, "Cavity resonance suppression using miniature fluidic oscillators," *AIAA J.* **42**, 2608–2612 (2004).
- ⁵G. Raman, S. Packiarajan, G. Papadopoulos, C. Weissman, and S. Raghu, "Jet thrust vectoring using a miniature fluidic oscillator," *Aeronaut. J.* **109**, 129–138 (2005).
- ⁶S. Roux, M. Fénot, G. Lalizel, L.-E. Brizzi, and E. Dornigac, "Experimental investigation of the flow and heat transfer of an impinging jet under acoustic excitation," *Int. J. Heat Mass Transfer* **54**, 3277–3290 (2011).
- ⁷J. M. Wiltse and A. Glezer, "Manipulation of free shear flows using piezoelectric actuators," *J. Fluid Mech.* **249**, 261–285 (1993).
- ⁸D. Rapoport, I. Fono, K. Cohen, and A. Seifert, "Closed-loop vectoring control of a turbulent jet using periodic excitation," *J. Propul. Power* **19**, 646–654 (2003).
- ⁹J. W. S. Rayleigh, *The Theory of Sound Perception* (Macmillan, 1896).
- ¹⁰P. T. Nagy and G. Paál, "Modeling the perturbation growth in an acoustically excited plane jet," *Phys. Fluids* **29**, 114102 (2017).
- ¹¹M. Mair, M. Bacic, K. Chakravarthy, and B. Williams, "Jet preferred mode vs shear layer mode," *Phys. Fluids* **32**, 064106 (2020).
- ¹²G. Arwatz, I. Fono, and A. Seifert, "Suction and oscillatory blowing actuator modeling and validation," *AIAA J.* **46**, 1107–1117 (2008).
- ¹³S. Wang, A. Batikh, L. Baldas, A. Kourta, N. Mazellier, S. Colin, and S. Orioux, "On the modelling of the switching mechanisms of a Coanda fluidic oscillator," *Sens. Actuators, A* **299**, 111618 (2019).
- ¹⁴G. Saliba, V. Raimbault, A. Batikh, S. Colin, and L. Baldas, "Relaxation fluidic oscillators: Design parameters, new operating modes and characteristics of their internal and external flows," *J. Fluids Eng.* **145**, 101202 (2023).
- ¹⁵C. J. Nicholls, B. M. T. Tang, J. Turner, and M. Bacic, "Novel operating mode of a fluidic oscillator," *J. Fluids Eng.* **144**, 071501 (2022).
- ¹⁶J. W. Gregory, E. P. Gnanamanickam, J. P. Sullivan, and S. Raghu, "Variable-frequency fluidic oscillator driven by a piezoelectric bender," *AIAA J.* **47**, 2717–2725 (2009).
- ¹⁷D. Culley, "Variable frequency diverter actuation for flow control," AIAA Paper No. AIAA 2006-3034, 2006.
- ¹⁸J. W. Gregory, J. Ruotolo, A. Byerley, and T. McLaughlin, "Switching behavior of a plasma-fluidic actuator," AIAA Paper No. AIAA 2007-785, 2007.
- ¹⁹M. Mair, M. Bacic, and P. Ireland, "On dynamics of acoustically driven bistable fluidic valves," *J. Fluids Eng.* **141**, 061202 (2019).
- ²⁰M. Mair and M. Bacic, "Fluid dynamics of a bistable diverter under ultrasonic excitation—Part I: Performance characteristic," *J. Fluids Eng.* **143**, 071201 (2021).
- ²¹M. Mair, M. Bacic, K. Chakravarthy, and B. Williams, "Fluid dynamics of a bistable diverter under ultrasonic excitation—Part II: Flow visualization and fundamental mechanisms," *J. Fluids Eng.* **143**, 071202 (2021).
- ²²C. J. Nicholls and M. Bacic, "Fluidic oscillator with active phase control," *AIAA J.* **61**, 1973–1985 (2023).
- ²³M. N. Tomac and E. T. Sundström, "Adjustable frequency fluidic oscillator with supermode frequency," *AIAA J.* **57**, 3349–3359 (2019).
- ²⁴M. N. Tomac and E. Sundström, "Fluidic oscillator with variable sweep and inclination angles," *AIAA J.* **58**, 1182–1193 (2020).
- ²⁵C. E. Spyropoulos, "A sonic oscillator," in *Proceedings of the Fluid Amplification Symposium*, Washington D.C. (Harry Diamond Laboratories, 1964), Vol. III, pp. 27–51.
- ²⁶N. D. Martin, M. Bottomley, and A. Packwood, "Switching of a bistable diverter valve with synthetic jet actuators," *AIAA J.* **52**, 1563–1568 (2014).
- ²⁷C. J. Nicholls and M. Bacic, "Closed-loop control of a piezo-fluidic amplifier," *AIAA J.* **58**, 2414–2427 (2020).
- ²⁸H. Coandă, "Device for deflecting a stream of elastic fluid projected into an elastic fluid," U.S. patent 2,052,869 (1936).

- ²⁹C. Bourque and B. G. Newman, "Reattachment of a two-dimensional, incompressible jet to an adjacent flat plate," *Aeronaut. Q.* **11**, 201–232 (1960).
- ³⁰D. R. Chapman, D. M. Kuehn, and H. K. Larson, "Investigation of separated flows in supersonic and subsonic streams with emphasis on the effect of transition," Technical Report No. NACA-TR-1356 (NASA, 1957).
- ³¹H. Görtler, "Berechnung von aufgaben der freien turbulenz auf grund eines neuen näherungsansatzes," *Z. Angew. Math. Mech.* **22**, 244–254 (1942).
- ³²R. A. Sawyer, "Two-dimensional reattaching jet flows including the effects of curvature on entrainment," *J. Fluid Mech.* **17**, 481–498 (1963).
- ³³H. Reichardt, *Gesetzmäßigkeiten der Freien Turbulenz* (VDI-Forschungsheft, 1942).
- ³⁴H. R. Muller, "A study of the dynamic features of a wall-reattachment fluid amplifier," *J. Basic Eng.* **86**, 819–826 (1964).
- ³⁵P. A. Lush, "Investigation of the switching mechanism in a large scale model of a turbulent reattachment amplifier," in 2nd Cranfield Fluidics Conference, Cambridge, UK, 1967.
- ³⁶P. A. Lush, "A theoretical and experimental investigation of the switching mechanism in a wall attachment fluid amplifier," in IFAC Symposium on Fluidics, 1968.
- ³⁷R. A. Sawyer, "The flow due to a two-dimensional jet issuing parallel to a flat plate," *J. Fluid Mech.* **9**, 543–559 (1960).
- ³⁸S. G. Levin and F. M. Manion, "Jet attachment distance as a function of adjacent wall offset and angle," Technical Report No. 1087 (Harry Diamond Laboratories, 1962).
- ³⁹H. W. Chang, "Dynamic analysis of a monostable fluid amplifier," Ph.D. thesis (Oklahoma State University, 1978).
- ⁴⁰J. M. Goto and T. M. Drzewiecki, "An analytical model for the response of flue-ric wall attachment amplifiers," Report No. HDL-TR-1598 (Harry Diamond Laboratories, 1972).
- ⁴¹M. Epstein, "Theoretical investigation of the switching mechanism in a bistable wall attachment fluid amplifier," *J. Basic Eng.* **93**, 55–62 (1971).
- ⁴²J. M. Kirshner and S. Katz, *Design Theory of Fluidic Components* (Academic Press, 2012).
- ⁴³S. C. Crow and F. H. Champagne, "Orderly structure in jet turbulence," *J. Fluid Mech.* **48**, 547–591 (1971).
- ⁴⁴K. B. M. Q. Zaman and A. K. M. F. Hussain, "Vortex pairing in a circular jet under controlled excitation. Part 1. General jet response," *J. Fluid Mech.* **101**, 449–491 (1980).
- ⁴⁵J. Davitian, C. Hendrickson, D. Getsinger, R. T. M'Closkey, and A. R. Karagozian, "Strategic control of transverse jet shear layer instabilities," *AIAA J.* **48**, 2145–2156 (2010).
- ⁴⁶C. J. Nicholls, K. Chakravarthy, B. M. T. Tang, B. A. O. Williams, and M. Bacic, "On acoustically modulated jet shear layers and the Nyquist–Shannon sampling theorem," *Phys. Fluids* **34**, 115106 (2022).
- ⁴⁷B. P. Lathi and D. Zhi, *Modern Digital and Analog Communication Systems* (Oxford University Press, Inc., 1995).
- ⁴⁸C. J. Nicholls, K. Chakravarthy, B. M. T. Tang, B. A. O. Williams, and M. Bacic, "Shear layer response to overmodulated acoustic perturbations," *Phys. Fluids* **35**, 015113 (2023).
- ⁴⁹J. P. Ries, "Dynamic modeling of the bistable fluid amplifier," Technical Report No. AD743201 (Lehigh University, Bethlehem, PA, 1972).
- ⁵⁰C. Nicholls, "The analysis, modelling, and acoustic control of fluidic devices," Ph.D. thesis (University of Oxford, 2021).
- ⁵¹R. L. Harrison, "Introduction to Monte Carlo simulation," *AIP Conf. Proc.* **1204**, 17–21 (2010).
- ⁵²E. Förthmann, "Über turbulente strahlausbreitung," *Ing.-Arch.* **5**, 42–54 (1934).
- ⁵³J. Boussinesq, *Essai Sur la Théorie des Eaux Courantes* (Imprimerie Nationale, 1877).